MODERN ANTENNA HANDBOOK

Edited by

Constantine A. Balanis

WILEY

A JOHN WILEY & SONS, INC., PUBLICATION

Published by John Wiley & Sons, Inc.
Published simultaneously in Canada

Library of Congress Cataloging-in-Publication Data:

Balanis, Constantine A., 1938–
Modern antenna handbook / Constantine A. Balanis.
p. cm.
Includes index.
ISBN 978-0-470-03634-1 (cloth)
1. Antennas (Electronics) I. Title.
TK7871.6.B354 2008
621.382′4—dc22

2007050162

Printed in the United States of America

10 9 8 7 6 5 4 3 2 1

CHAPTER 19

Near-Field Scanning Measurements: Theory and Practice

MICHAEL H. FRANCIS and RONALD C. WITTMANN

19.1 INTRODUCTION

As antennas increase in size or operating frequency, it becomes increasingly difficult to obtain adequate real estate to measure antenna properties in the far field. Typically, a distance of nD^2/λ is specified as the beginning of the far-field region, where n is often 2 for routine work, D is the diameter of the smallest sphere that encloses the antenna's radiating parts, and λ is the wavelength. At this distance and for a spherical wavefront, the phase differs by $\pi/8$ between the center and edge of the antenna. For precision measurements, n often must be much greater than 2 [1, Chap. 14]. Table 19.1 shows the far-field distances for some sample antenna diameters and operating frequencies. We see that even for antennas of modest size, the far-field distance can become prohibitively large when the frequency is high enough. Thus there are situations where measuring an antenna in the near field would be advantageous because large amounts of real estate are not required. There are other advantages as well. Since the near-field method is usually employed inside a chamber, it is not subject to the effects of the weather and also provides a more secure environment.

Determining the far-field pattern of an antenna from near-field measurements requires a mathematical transformation and correction for the characteristics of the measuring antenna (hereafter referred to as the probe). The first efficient near-field-to-far-field transformation for the planar geometry was developed by Kerns and Dayhoff [2] at the National Bureau of Standards (now the National Institute of Standards and Technology). Subsequently Kerns [3, 4] introduced probe correction. (Probe correction was developed earlier for a two-dimensional case (scanning on a circle) by Brown and Jull [5].) Within a few years the transformations were formulated for the spherical geometry by Jensen [6, 7] and Larsen [8] at the Technical University of Denmark. Wacker [9] of the National Bureau of Standards also made important contributions to the early development of spherical near-field scanning. The cylindrical transformation was developed, using reciprocity, by Leach and Paris [10–11] at the Georgia Institute of Technology. Subsequently, Yaghjian [12] at the National Bureau of Standards elaborated the cylindrical

Modern Antenna Handbook. Edited by Constantine A. Balanis

TABLE 19.1 Sample Far-Field Distances

Diameter (m)	Frequency (GHz)	Far-Field Distance (m)
1	3	20
3	3	180
10	3	2000
1	30	200
3	30	1800
10	30	20000
1	100	667
3	100	6000
10	100	66700

transformation based on a scattering-matrix approach. A detailed history of the development of near-field scanning methods can be found in Gillespie [13], especially the papers by Baird et al. [14], Hansen and Jensen [15], and Joy [16]. An extensive bibliography is given in these historical papers and also in Yaghjian [17]. A good, complementary reference that also treats all three geometries is Appel-Hansen et al. [18].

In principle, it is possible to transform to the far-field from measurements made on an arbitrary near-field surface. However, the transformation can be done efficiently for only three scanning geometries: planar (Section 19.2.3), spherical (Section 19.2.4), and Cylindrical (Section 19.2.5). These transformations require complex data (amplitude and phase).

19.2 NEAR-FIELD MEASUREMENT THEORY

19.2.1 Overview

Near-field measurement methods require the development of formulas that describe the coupling of two antennas in close proximity. Avoiding the polarization issue for now, we outline the process using the simpler example of a scalar field $u(\mathbf{r})$. (Near-field scanning measurements have also been developed for applications in acoustics [19–22].)

First, we expand the field of the test antenna in a complete set of modes $u_n(\mathbf{r})$:

$$u(\mathbf{r}) = a_0 \sum_{n=1}^{N} t_n u_n(\mathbf{r}) \tag{19.1}$$

where a_0 is the excitation. (In cases where modes are not discrete, the sum is replaced by an integral.) It must be possible to represent $u(\mathbf{r})$ to acceptable accuracy by use of a finite summation. The expansion (19.1) must be valid throughout the region of interest, including the region where measurements are made.

Practical probes do not (or only approximately) measure the field at a point in space. This fact is especially important near a source where fields may vary significantly over the volume of the probe. To account for probe effects, it is necessary to catalog the response of the probe to each mode in the expansion (19.1):

$$w_n'(\mathbf{r}', \mathbf{R}') = [\mathcal{P}u_n]\left(\mathbf{r}', \mathbf{R}'\right) \tag{19.2}$$

where the arguments must specify probe position (location and orientation). In this case, the vector $\mathbf{r}'$ gives the location and the matrix $\mathbf{R}'$ (Section 19.2.2.2.) determines the orientation. The probe is represented as a linear operator $\mathcal{P}$. (The probe can be modeled effectively as a differential operator [23], [24, Chap. 8]). As discussed in subsequent sections, w_n' can be calculated from the known receiving function of the probe.

The response of the probe to the field in Eq. (19.1) can be approximated as a superposition of the responses of the probe to the contributing modes:

$$\frac{w'(\mathbf{r}, \mathbf{R})}{a_0} = \sum_{n=1}^{N} w_n'(\mathbf{r}, \mathbf{R}) t_n \tag{19.3}$$

We assume that the presence of the probe does not affect the test-antenna field. Discrepancies due to probe–test antenna interaction are called multiple-reflection or mutual-coupling errors. (Multiple reflections are accounted for in developments that use a full scattering-matrix theory [12, 25, 26]; however, practical implementations (so far) retain only the direct interaction term discussed here.)

To determine the coefficients t_n we can, in principle, make independent measurements at the probe positions (locations and orientations) $(\mathbf{r}_i, \mathbf{R}_i)$, $1 \leq i \leq P$, $P \geq N$, and find the least-squares solution of the system of linear equations generated from the *transmission equation* (19.3). This would require $O(N^3)$ operations using, for example, Gaussian elimination. For many practical antenna problems $10^4 < N < 10^6$ and computational efficiency is a major concern. For this reason, near-field measurements are commonly made so that data points lie on planar, spherical, or cylindrical surfaces. The separation of coordinates, orthogonalities, and simple rotational and translational properties, which characterize the modes in these geometries, allow for significant reduction in processing time. Computational complexity is $O(N \log N)$ for the planar and cylindrical geometries, and $O(N^{3/2})$ for the spherical geometry. (Recent developments [27] suggest the possibility of a practical $O(N \log N)$ algorithm for spherical scanning.)

As separation increases, the coupling between test antenna and probe reduces to a simple asymptotic form. The resulting simpler theory (Friis transmission equation) and data acquisition requirements are the primary motivations for making *far-field measurements*. For electrically large antennas, however, obtaining adequate separation may not be practical. Additionally, the ability to use smaller separation distances means that many antenna measurements can be made within a controlled laboratory environment. This fact may result in improved security and accuracy.

Theory presented here represents a mathematical ideal. An effective, practical implementation requires the spirit of intelligent compromise that embodies the "art" of measurement.

19.2.2 General Considerations

19.2.2.1 Maxwell's Equations and Plane Waves We consider time-harmonic fields with frequency $f = \omega/2\pi$, wavenumber $k = 2\pi/\lambda$, and wavelength λ. (Time domain near-field measurements are discussed in [28].) The time-dependent factor $\exp(-i\omega t)$ is suppressed. In free space, the complex electromagnetic fields obey the equations

$$\nabla \cdot \mathbf{E}(\mathbf{r}) = \nabla \cdot \mathbf{H}(\mathbf{r}) = 0 \tag{19.4}$$

$$\frac{1}{k}\nabla \times \mathbf{E}(\mathbf{r}) = iZ_0\mathbf{H}(\mathbf{r})$$
$$\frac{1}{k}\nabla \times \mathbf{H}(\mathbf{r}) = \frac{1}{iZ_0}\mathbf{E}(\mathbf{r}) \tag{19.5}$$

The impedance of free space is $Z_0 = \sqrt{\mu_0/\varepsilon_0} \approx 377\ \Omega$. In particular, *the electric and magnetic fields each satisfy the Helmholtz equation*:

$$(\nabla^2 + k^2)\mathbf{E}(\mathbf{r}) = \mathbf{0} \tag{19.6}$$
$$(\nabla^2 + k^2)\mathbf{H}(\mathbf{r}) = \mathbf{0}$$

Perhaps the simplest solution of Eqs. (19.4)–(19.6) is the plane wave,

$$\mathbf{E}_{\text{pw}}(\mathbf{r}) = \frac{1}{2\pi}\mathbf{A}(\hat{\mathbf{k}})\exp(i\mathbf{k}\cdot\mathbf{r}) \tag{19.7}$$
$$\mathbf{H}_{\text{pw}}(\mathbf{r}) = \frac{1}{iZ_0}i\hat{\mathbf{k}} \times \mathbf{E}_{\text{pw}}(\mathbf{r})$$

where

$$\mathbf{k}\cdot\mathbf{A}(\hat{\mathbf{k}}) = 0 \tag{19.8}$$
$$\mathbf{k}\cdot\mathbf{k} = k^2 \tag{19.9}$$
$$\hat{\mathbf{k}} = \mathbf{k}/k \tag{19.10}$$

When $\mathbf{k}$ is real, $\mathbf{E}_{\text{pw}}$ is organized into planes of constant phase that are perpendicular to $\mathbf{k}$. These phase fronts propagate in the $\mathbf{k}$ direction at the speed of light $c = \lambda f \approx 3 \times 10^8$ m/s. We define the unit vector corresponding to $\mathbf{a}$ as $\hat{\mathbf{a}} = \mathbf{a}/\sqrt{\mathbf{a}\cdot\mathbf{a}}$ so that $\hat{\mathbf{a}}\cdot\hat{\mathbf{a}} = \mathbf{1}$; however, $\hat{\mathbf{a}}\cdot\hat{\mathbf{a}}^* \neq 1$ when $\mathbf{a}$ is complex.

19.2.2.2 Coordinate Systems The laboratory system is specified by the set $(\mathbf{O}, \hat{\mathbf{x}}, \hat{\mathbf{y}}, \hat{\mathbf{z}})$, where $\mathbf{O}$ is the origin and the unit vectors $\hat{\mathbf{x}}$, $\hat{\mathbf{y}}$, and $\hat{\mathbf{z}}$ give the directions of the x, y, and z axes in a right-handed Cartesian coordinate system. We also embed a local Cartesian coordinate system $(\mathbf{O}_0, \hat{\mathbf{x}}_0, \hat{\mathbf{y}}_0, \hat{\mathbf{z}}_0)$ in an antenna. The location of the antenna is given by the coordinates of the point $\mathbf{O}_0$ in the laboratory coordinate system. The orientation of the antenna is defined by expressing $\hat{\mathbf{x}}_0$, $\hat{\mathbf{y}}_0$, and $\hat{\mathbf{z}}_0$ in terms of $\hat{\mathbf{x}}$, $\hat{\mathbf{y}}$, and $\hat{\mathbf{z}}$; for example, $\hat{\mathbf{x}}_0 = \mathbf{R}\hat{\mathbf{x}}$, $\hat{\mathbf{y}}_0 = \mathbf{R}\hat{\mathbf{y}}$, and $\hat{\mathbf{z}}_0 = \mathbf{R}\hat{\mathbf{z}}$, where $\mathbf{R}$ is the 3×3 matrix (Cartesian basis) that induces a specified rotation [29, Eq. (C.45)].

The *minimum sphere* is the smallest sphere, centered on $\mathbf{O}_0$, that encloses the antenna. The mathematical description of an antenna is most efficient if $\mathbf{O}_0$ is chosen so that the minimum sphere is as small as possible. Additionally, we assume that $\hat{\mathbf{z}}_0$ *is directed away from the antenna*, usually along an axis of mechanical symmetry. This axis often corresponds closely to the axis of maximum gain or effective area. See Figures 19.1 and 19.18.

The term *reference position* is used to describe the state $(\mathbf{O}_0, \hat{\mathbf{x}}_0, \hat{\mathbf{y}}_0, \hat{\mathbf{z}}_0) = (\mathbf{O}, \hat{\mathbf{x}}, \hat{\mathbf{y}}, \hat{\mathbf{z}})$ for the test antenna and $(\mathbf{O}'_0, \hat{\mathbf{x}}'_0, \hat{\mathbf{y}}'_0, \hat{\mathbf{z}}'_0) = (z'\hat{\mathbf{z}}, -\hat{\mathbf{x}}, \hat{\mathbf{y}}, -\hat{\mathbf{z}})$ for the probe. When the test antenna and probe are in their reference positions, they face each other along the laboratory z axis (Figure 19.1). For any valid z', there will be a plane $z = z_0$ such that the test antenna is contained in the region $z < z_0$ and the probe is contained in the region $z > z_0$. It is convenient to begin in the reference positions when describing the translations and rotations that effectively move the probe over the measurement surface. (In some near-field scanning implementations, the test antenna rotates in the laboratory coordinate system. See Figure 19.14, for example.)

19.2.2.3 Waveguide Feeds We assume that an antenna is coupled to a generator or to a load through a single-moded, lossless waveguide feed (which may be coaxial). Phase is measured relative to a reference plane that is usually located at the point (waveguide port) where the antenna connects to the RF system. See Refs. 25 and 30 for a complete discussion of waveguide circuit theory.

The power accepted by a transmitting antenna is

$$P_0 = K|a_0|^2\left(1 - |\Gamma|^2\right) \tag{19.11}$$

where a_0 is the (complex) amplitude of the incident waveguide mode and Γ is the reflection coefficient looking into the antenna through its feed.

The constant of proportionality K is arbitrary since it depends on the normalization chosen for the waveguide modes. Once K is specified, $|a_0|$ can be uniquely determined by a measurement of power. (The phase of a_0 is often not important.) For convenience we use

$$K = \frac{1}{2k^2 Z_0} \tag{19.12}$$

Thus a_0 has the dimension V/m.

19.2.2.4 Transmitting and Receiving Functions Far from an antenna that is transmitting, the radiated electromagnetic fields can be characterized simply:

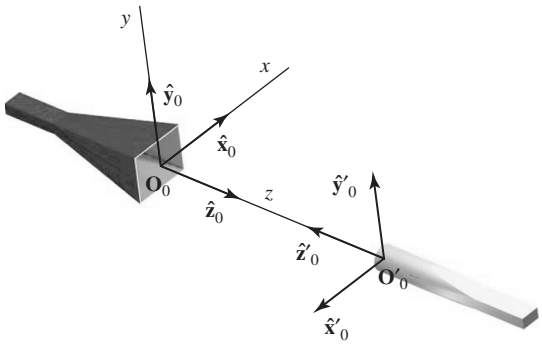

Figure 19.1 A test antenna and a probe in their reference positions in the laboratory coordinate system; that is, $(\mathbf{O}_0, \hat{\mathbf{x}}_0, \hat{\mathbf{y}}_0, \hat{\mathbf{z}}_0) = (\mathbf{O}, \hat{\mathbf{x}}, \hat{\mathbf{y}}, \hat{\mathbf{z}})$ and $\left(\mathbf{O}'_0, \hat{\mathbf{x}}'_0, \hat{\mathbf{y}}'_0, \hat{\mathbf{z}}'_0\right) = \left(z'\hat{\mathbf{z}}, -\hat{\mathbf{x}}, \hat{\mathbf{y}}, -\hat{\mathbf{z}}\right)$.

$$\begin{aligned}\mathbf{E}(\mathbf{r}) &\underset{r\to\infty}{\sim} a_0\mathbf{t}(\hat{\mathbf{r}})\frac{\exp(ikr)}{ikr}, \qquad \hat{\mathbf{r}}\cdot\mathbf{t}(\hat{\mathbf{r}}) = 0 \\ \mathbf{H}(\mathbf{r}) &\underset{r\to\infty}{\sim} \frac{1}{iZ_0} i\hat{\mathbf{r}}\times\mathbf{E}(\mathbf{r})\end{aligned} \tag{19.13}$$

The *transmitting function* $\mathbf{t}(\hat{\mathbf{r}})$ depends only on direction, which is specified by the unit vector $\hat{\mathbf{r}}$.

Next, consider a plane wave (Eq. (19.7))

$$\mathbf{E}_{\text{pw}}(\mathbf{r}) = \frac{1}{2\pi}\mathbf{A}(\hat{\mathbf{k}})\exp(i\mathbf{k}\cdot\mathbf{r})$$

that is incident on an antenna that is receiving. The *receiving function* $\mathbf{s}(\hat{\mathbf{k}})$ is defined so that the received signal is

$$w = (1 - \Gamma\Gamma_\ell)b_0 = \mathbf{s}(\hat{\mathbf{k}})\cdot\mathbf{A}(\hat{\mathbf{k}}) \tag{19.14}$$

Here, b_0 is the (complex) amplitude of the emergent waveguide mode and Γ_ℓ is the reflection coefficient of the load; that is, w is the amplitude of the emergent waveguide mode that would be present were the load nonreflecting.

The forms of the functions $\mathbf{t}$ and $\mathbf{s}$ depend on the position (location and orientation) of the antenna in the laboratory coordinate system. For the special case $(\mathbf{O}_0, \hat{\mathbf{x}}_0, \hat{\mathbf{y}}_0, \hat{\mathbf{z}}_0) = (\mathbf{O}, \hat{\mathbf{x}}, \hat{\mathbf{y}}, \hat{\mathbf{z}})$ in which the antenna is located at the origin and is pointed in the $\hat{\mathbf{z}}$ direction, we add a subscript 0, so that

$$\mathbf{t}(\hat{\mathbf{k}}) \to \mathbf{t}_0(\hat{\mathbf{k}}), \quad \mathbf{s}(\hat{\mathbf{k}}) \to \mathbf{s}_0(\hat{\mathbf{k}}) \tag{19.15}$$

For the special case $(\mathbf{O}_0, \hat{\mathbf{x}}_0, \hat{\mathbf{y}}_0, \hat{\mathbf{z}}_0) = (\mathbf{O}, -\hat{\mathbf{x}}, \hat{\mathbf{y}}, -\hat{\mathbf{z}})$ in which the antenna is located at the origin and is pointed in the $-\hat{\mathbf{z}}$ direction, we add a subscript π, so that

$$\mathbf{t}(\hat{\mathbf{k}}) \to \mathbf{t}_\pi(\hat{\mathbf{k}}), \quad \mathbf{s}(\hat{\mathbf{k}}) \to \mathbf{s}_\pi(\hat{\mathbf{k}}) \tag{19.16}$$

The functions $\mathbf{t}_\pi(\hat{\mathbf{r}})$ and $\mathbf{s}_\pi(\hat{\mathbf{r}})$ can be obtained by rotating $\mathbf{t}_0(\hat{\mathbf{r}})$ and $\mathbf{s}_0(\hat{\mathbf{r}})$ by 180° about the laboratory y axis.

In accordance with our conventions, we may take

$$\mathbf{s}(\hat{\mathbf{k}}) = \mathbf{t}(-\hat{\mathbf{k}}) \tag{19.17}$$

when an antenna is *reciprocal*. See Kerns [25, Chap. II, Appendix A] for a detailed discussion of reciprocity.

19.2.2.5 Basic Antenna Parameters Following IEEE Standard 145-1993 [31], the *gain* $G(\hat{\mathbf{r}})$ and *effective area* $\sigma(\hat{\mathbf{r}})$ of an antenna are

$$G(\hat{\mathbf{r}}) = \frac{4\pi}{1 - |\Gamma|^2}\,\|\mathbf{t}_0(\hat{\mathbf{r}})\|^2 \tag{19.18}$$

$$\sigma(\hat{\mathbf{r}}) = \frac{\lambda^2}{1 - |\Gamma|^2} \|\mathbf{s}_0(\hat{\mathbf{r}})\|^2 \tag{19.19}$$

When an antenna is reciprocal (Eq. (19.17)),

$$\sigma(\hat{\mathbf{r}}) = \frac{\lambda^2}{4\pi} G(-\hat{\mathbf{r}}) \tag{19.20}$$

We use the term *pattern* to refer to a transmitting or receiving "function" of unspecified normalization. Any pattern can be normalized to satisfy Eq. (19.18) or (19.19) if Γ is known and if the gain or effective area is available in some direction.

The *directivity* $D(\hat{\mathbf{r}})$ is given by

$$D(\hat{\mathbf{r}}) = G(\hat{\mathbf{r}}) \frac{P_0}{P_T} = \frac{4\pi}{\int_0^{2\pi} \int_0^{\pi} \|\mathbf{t}_0(\hat{\mathbf{r}})\|^2 \sin\theta \, d\theta \, d\varphi} \|\mathbf{t}_0(\hat{\mathbf{r}})\|^2 \tag{19.21}$$

where P_T is the total radiated power. Due to ohmic losses, $P_T < P_0$ and so $G(\hat{\mathbf{r}}) < D(\hat{\mathbf{r}})$. Equation (19.21) holds regardless of the normalization used for the pattern. Calculation of directivity in planar or cylindrical scanning is subject to truncation error because the measurement surfaces never completely enclose the test antenna. Spherical scanning, however, provides the simple result (see Eq. (19.60))

$$\int_0^{2\pi} \int_0^{\pi} \|\mathbf{t}_0(\hat{\mathbf{r}})\|^2 \sin\theta \, d\theta \, d\varphi = \sum_{nm} \left(\left| t_{nm}^1 \right|^2 + \left| t_{nm}^2 \right|^2 \right) \tag{19.22}$$

In addition to the above parameters, the *equivalent isotropic radiated power* (EIRP) [31]

$$EIRP(\hat{\mathbf{r}}) = G(\hat{\mathbf{r}}) P_0 \tag{19.23}$$

is often of interest, particularly for communication satellite applications. Near-field measurement of EIRP may require a specialized technique since the antenna's waveguide port is not accessible in some systems [32].

19.2.2.6 Miscellaneous Conventions We assume the "standard" branch when specifying square roots; that is, if

$$a + ib = \sqrt{x + iy}$$

then $a \geq 0$, $b \geq 0$ when $y \geq 0$, and $b < 0$ when $y < 0$. In particular, *the square root of a nonzero real number is either positive real or positive imaginary*.

Quantities associated with a probe are marked with primes (single or double) when such distinctions are desirable.

In this development, the probe always receives and the test antenna always transmits. Transmission equations for transmitting probes and receiving test antennas may be found by straightforward generalization of our arguments. For the convenience of the reader, however, Appendix A lists transmission equations for transmitting probes and receiving test antennas.

For the most part, theories of near-field planar, spherical, and cylindrical scanning have developed independently. We have attempted to bring some uniformity to the notation. Here, for example, (1) modal functions are dimensionless, (2) pattern functions (and the scattering matrix, in general) are dimensionless, and (3) the modal coefficients carry the dimensions of the electric field (V/m).

19.2.3 Planar Scanning

19.2.3.1 Plane Wave Representation Scalar solutions of Eq. (19.6), separated in Cartesian coordinates (Figure 19.2), are given by plane waves

$$\begin{aligned} u_{\alpha\beta}(\mathbf{r}) &= \frac{1}{2\pi}\exp(i\mathbf{k}\cdot\mathbf{r}) \\ &= \frac{1}{2\pi}\exp(i\alpha x + i\beta y)\exp(i\gamma z) \end{aligned} \tag{19.24}$$

where

$$\mathbf{k}\cdot\mathbf{k} = k^2$$

In Eq. (19.24) we restrict $\mathbf{k}$ so that

$$\begin{gathered} k_x = \alpha, \quad k_y = \beta, \quad k_z = \gamma \\ -\infty < \alpha, \beta < \infty \\ \gamma = \sqrt{k^2 - \alpha^2 - \beta^2} \end{gathered} \tag{19.25}$$

In formulas where α, β, or γ appear explicitly, it is to be understood that $\mathbf{k} = \alpha\hat{\mathbf{x}} + \beta\hat{\mathbf{y}} + \gamma\hat{\mathbf{z}}$.

When γ is real (corresponding to $k^2 > \alpha^2 + \beta^2$), $u_{\alpha\beta}(\mathbf{r})$ describes a plane wave that propagates into the half-space $z > z_0$. When γ is imaginary (corresponding to $k^2 < \alpha^2 + \beta^2$), $u_{\alpha\beta}(\mathbf{r})$ is an "evanescent" wave that decays exponentially as z increases. When

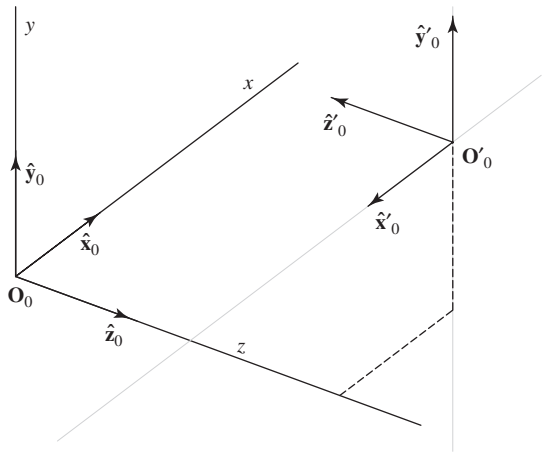

Figure 19.2 Planar scanning geometry. The scan plane is $z = d$. The test antenna is in its reference position (see Figure 19.1). The probe is shown at the position (x, y, z) with $x = d/2$, $y = d/2$, and $z = d$. Furthermore, $\hat{\mathbf{x}}'_0 = -\hat{\mathbf{x}}$, $\hat{\mathbf{y}}'_0 = \hat{\mathbf{y}}$, and $\hat{\mathbf{z}}'_0 = -\hat{\mathbf{z}}$.

sources are confined to the region $z < z_0$, the functions $u_{\alpha\beta}(\mathbf{r})$ form a complete basis for representing fields in the free-space region $z > z_0$.

Vector solutions of Eqs. (19.4) and (19.6) follow directly from the scalar solutions (Eq. (19.24)):

$$\begin{aligned} \mathbf{m}_{\alpha\beta}(\mathbf{r}) &= \frac{1}{k}\nabla \times \mathbf{n}_{\alpha\beta}(\mathbf{r}) = u_{\alpha\beta}(\mathbf{r})\mathbf{e}^1(\hat{\mathbf{k}}) \\ \mathbf{n}_{\alpha\beta}(\mathbf{r}) &= \frac{1}{k}\nabla \times \mathbf{m}_{\alpha\beta}(\mathbf{r}) = u_{\alpha\beta}(\mathbf{r})\mathbf{e}^2(\hat{\mathbf{k}}) \end{aligned} \tag{19.26}$$

$$\hat{\mathbf{k}} \cdot \mathbf{m}_{\alpha\beta}(\mathbf{r}) = \hat{\mathbf{k}} \cdot \mathbf{n}_{\alpha\beta}(\mathbf{r}) = 0 \tag{19.27}$$

Here,

$$\begin{aligned} \mathbf{e}^1(\hat{\mathbf{r}}) &= \begin{cases} \dfrac{\hat{\mathbf{z}} \times \hat{\mathbf{r}}}{\sqrt{1 - (\hat{\mathbf{z}} \cdot \hat{\mathbf{r}})^2}}, & \hat{\mathbf{r}} \neq \pm\hat{\mathbf{z}} \\ \pm\hat{\mathbf{y}}, & \hat{\mathbf{r}} = \pm\hat{\mathbf{z}} \end{cases} \\ \mathbf{e}^2(\hat{\mathbf{r}}) &= i\hat{\mathbf{r}} \times \mathbf{e}^1(\hat{\mathbf{r}}) \end{aligned} \tag{19.28}$$

Equation (19.27) is a direct restatement of Eq. (19.4).

The electromagnetic fields of a test antenna (in the reference position) can be expanded as

$$\begin{aligned} \mathbf{E}(\mathbf{r}) &= a_0 \int_{-\infty}^{\infty}\int_{-\infty}^{\infty} \left[t^1_{\alpha\beta}\mathbf{m}_{\alpha\beta}(\mathbf{r}) + t^2_{\alpha\beta}\mathbf{n}_{\alpha\beta}(\mathbf{r})\right] \frac{d\alpha\, d\beta}{\gamma k} \\ iZ_0\mathbf{H}(\mathbf{r}) &= a_0 \int_{-\infty}^{\infty}\int_{-\infty}^{\infty} \left[t^2_{\alpha\beta}\mathbf{m}_{\alpha\beta}(\mathbf{r}) + t^1_{\alpha\beta}\mathbf{n}_{\alpha\beta}(\mathbf{r})\right] \frac{d\alpha\, d\beta}{\gamma k}, \quad z > z_0 \end{aligned} \tag{19.29}$$

When γ is real,

$$\frac{d\alpha\, d\beta}{\gamma k} \to \sin\theta\, d\theta\, d\varphi \tag{19.30}$$

so that $d\alpha\, d\beta/\gamma k$ is a differential solid angle. For $\alpha^2 + \beta^2 > k^2$, the integrand in Eq. (19.29) is exponentially attenuated with increasing $|\gamma|$. The resulting bandlimit has important consequences in the practical implementation of the theory.

We write

$$\mathbf{t}_0(\hat{\mathbf{k}}) = t^1_{\alpha\beta}\mathbf{e}^1(\hat{\mathbf{k}}) + t^2_{\alpha\beta}\mathbf{e}^2(\hat{\mathbf{k}}) \tag{19.31}$$

and, following Kerns [25] and Yaghjian [33, Eq. 8],

$$\mathbf{E}(\mathbf{r}) = \frac{a_0}{2\pi}\int_{-\infty}^{\infty}\int_{-\infty}^{\infty} \mathbf{t}_0\left(\hat{\mathbf{k}}\right) \exp(i\mathbf{k} \cdot \mathbf{r}) \frac{d\alpha\, d\beta}{\gamma k}, \quad z > z_0 \tag{19.32}$$

Equation (19.32) is a superposition of vector plane waves of the form in Eq. (19.7) in which $\mathbf{k}$ is restricted according to Eq. (19.25), so that $k_z = \gamma$ is positive real or positive imaginary.

A stationary-phase evaluation of Eq. (19.32) suggests the asymptotic result

$$\mathbf{E}(\mathbf{r}) \underset{r\to\infty}{\sim} a_0 \mathbf{t}_0(\hat{\mathbf{r}}) \frac{\exp(ikr)}{ikr} \tag{19.33}$$

that confirms $\mathbf{t}_0(\hat{\mathbf{r}})$ as the transmitting function. Equation (19.33) can be justified rigorously when the source is finite [34]. (A finite source can be enclosed within a sphere of finite radius.)

The transverse field is

$$\mathbf{E}_t(\mathbf{r}) = \mathbf{E}(\mathbf{r}) - \hat{\mathbf{z}}\hat{\mathbf{z}} \cdot \mathbf{E}(\mathbf{r}) = \frac{a_0}{2\pi} \int_{-\infty}^{\infty} \int_{-\infty}^{\infty} \mathbf{t}_t(\hat{\mathbf{k}}) \exp(i\mathbf{k} \cdot \mathbf{r}) \frac{d\alpha\, d\beta}{\gamma k} \tag{19.34}$$

This is a two-dimensional Fourier transform that can be inverted to give

$$\mathbf{t}_t(\hat{\mathbf{k}}) = \frac{\gamma k}{2\pi} \int_{-\infty}^{\infty} \int_{-\infty}^{\infty} \frac{\mathbf{E}_t(\mathbf{r})}{a_0} \exp(-i\mathbf{k} \cdot \mathbf{r}) dx\, dy, \quad z = d > z_0 \tag{19.35}$$

Because $\hat{\mathbf{k}} \cdot \mathbf{t}_0(\hat{\mathbf{k}}) = 0$,

$$\mathbf{t}_0(\hat{\mathbf{k}}) = \frac{1}{\gamma} \mathbf{k} \times [\mathbf{t}_t(\hat{\mathbf{k}}) \times \hat{\mathbf{z}}] \tag{19.36}$$

Thus the transmitting function is determined by the transverse electric field on any plane $z = d > z_0$.

19.2.3.2 Probe Response We begin with the test antenna and probe in their reference positions. In planar scanning, the response of the probe is recorded as the probe is translated (no rotation allowed) over the measurement plane $z = z' = d$. See Figure 19.1.

In the laboratory coordinate system, position (location and orientation) of the probe is described by the parameter set (x, y, z) with the probe reference position corresponding to $(0, 0, d)$. The position of a similarly translated test antenna is also described by these parameters with the test antenna reference position corresponding to $(0, 0, 0)$.

Consider the output when the test antenna is at its reference position and the probe is at (x', y', z'). The same output will be observed when the probe is at $(0, 0, 0)$ and the test antenna is at $(-x', -y', -z')$. This fact may be expressed mathematically as

$$w'(\mathbf{r}') = [\mathcal{P} \cdot \mathbf{E}](x', y', z') = [\mathcal{P} \cdot \tilde{\mathbf{E}}](0, 0, 0) \tag{19.37}$$

Here, $\mathcal{P}$ is a linear operator that represents the probe, $\mathbf{E}(\mathbf{r})$ is the field of the test antenna (at its reference position), and $\tilde{\mathbf{E}}(\mathbf{r})$ is the field of the translated test antenna.

Now, let the "test antenna" radiate the plane wave

$$\mathbf{E}_{\alpha\beta}(\mathbf{r}) = \frac{1}{2\pi} \mathbf{t}_0(\hat{\mathbf{k}}) \exp(i\mathbf{k} \cdot \mathbf{r})$$

so that

$$\tilde{\mathbf{E}}_{\alpha\beta}(\mathbf{r}) = \frac{1}{2\pi} \mathbf{t}_0(\hat{\mathbf{k}}) \exp[i\mathbf{k} \cdot (\mathbf{r} + \mathbf{r}')] = \mathbf{E}_{\alpha\beta}(\mathbf{r}) \exp(i\mathbf{k} \cdot \mathbf{r}') \tag{19.38}$$

From Eqs. (19.37) and (19.38)

$$w'_{\alpha\beta}(\mathbf{r}') = \exp(i\mathbf{k}\cdot\mathbf{r}')\left[\boldsymbol{\mathcal{P}}\cdot\mathbf{E}_{\alpha\beta}\right](0,0,0) \tag{19.39}$$

or

$$w'_{\alpha\beta}(\mathbf{r}') = \mathbf{s}'_{\pi}(\hat{\mathbf{k}})\cdot\mathbf{t}_0(\hat{\mathbf{k}})\exp(i\mathbf{k}\cdot\mathbf{r}') \tag{19.40}$$

where we have applied Eqs. (19.14) and (19.16). Equation (19.40) expresses the "obvious" fact that the output of a probe can vary only by a phase factor as it is translated from location to location in the presence of an incident (propagating) plane wave field. In the notation of Section 19.2.2.4,

$$\mathbf{s}'(\hat{\mathbf{k}}) = \mathbf{s}'_{\pi}(\hat{\mathbf{k}})\exp(i\mathbf{k}\cdot\mathbf{r}') \tag{19.41}$$

where $\mathbf{s}'(\hat{\mathbf{k}})$ is the receiving function of the translated probe at the location $\mathbf{r}'$.

19.2.3.3 Kerns Transmission Equation In Eq. (19.32) we have a modal expansion corresponding to Eq. (19.1). In Eq. (19.40) we have the response of the probe to each mode corresponding to Eq. (19.2). Finally, corresponding to Eq. (19.3), we have the *Kerns transmission formula* [25]

$$\frac{w'(\mathbf{r})}{a_0} = \int_{-\infty}^{\infty}\int_{-\infty}^{\infty}\mathbf{s}'_{\pi}(\hat{\mathbf{k}})\cdot\mathbf{t}_0(\hat{\mathbf{k}})\exp(i\mathbf{k}\cdot\mathbf{r})\frac{d\alpha\,d\beta}{\gamma k} \tag{19.42}$$

Equation (19.42) is valid when multiple reflections can be ignored and when the probe and test antenna can be physically separated by a plane perpendicular to $\hat{\mathbf{z}}$.

The Fourier transforms in Eq. (19.42) may be inverted to yield

$$\begin{aligned} T'_{\alpha\beta} &= \mathbf{s}'_{\pi}(\hat{\mathbf{k}})\cdot\mathbf{t}_0(\hat{\mathbf{k}}) = s^{1\prime}_{\alpha\beta}t^1_{\alpha\beta} - s^{2\prime}_{\alpha\beta}t^2_{\alpha\beta} \\ &= \frac{\gamma k}{4\pi^2}\int_{-\infty}^{\infty}\int_{-\infty}^{\infty}\frac{w'(\mathbf{r})}{a_0}\exp(-i\mathbf{k}\cdot\mathbf{r})dx\,dy, \quad z = d \end{aligned} \tag{19.43}$$

with Eq. (19.31) and

$$\mathbf{s}'_{\pi}(\hat{\mathbf{k}}) = s^{1\prime}_{\alpha\beta}\mathbf{e}^1(\hat{\mathbf{k}}) + s^{2\prime}_{\alpha\beta}\mathbf{e}^2(\hat{\mathbf{k}}) \tag{19.44}$$

Since $T'_{\alpha\beta}$ can be computed from data $w'(\mathbf{r})/a_0$ measured on the plane $z = d$, Eq. (19.43) provides one equation for the two unknown components of $\mathbf{t}_0(\hat{\mathbf{k}})$. Data from a second probe are needed to provide sufficient information to solve for $\mathbf{t}_0(\hat{\mathbf{k}})$. With two probes, we have the linear system

$$\begin{pmatrix} T'_{\alpha\beta} \\ \\ T''_{\alpha\beta} \end{pmatrix} = \begin{pmatrix} s^{1\prime}_{\alpha\beta} & -s^{2\prime}_{\alpha\beta} \\ \\ s^{1\prime\prime}_{\alpha\beta} & -s^{2\prime\prime}_{\alpha\beta} \end{pmatrix}\begin{pmatrix} t^1_{\alpha\beta} \\ \\ t^2_{\alpha\beta} \end{pmatrix} \tag{19.45}$$

Here, quantities associated with the second probe are marked with a double prime. Thus

$$\begin{pmatrix} t^1_{\alpha\beta} \\ \\ t^2_{\alpha\beta} \end{pmatrix} = \frac{-i}{\hat{\mathbf{k}}\cdot\left(\mathbf{s}'_{\pi}\times\mathbf{s}''_{\pi}\right)}\begin{pmatrix} -s^{2\prime\prime}_{\alpha\beta} & s^{2\prime}_{\alpha\beta} \\ \\ -s^{1\prime\prime}_{\alpha\beta} & s^{1\prime}_{\alpha\beta} \end{pmatrix}\begin{pmatrix} T'_{\alpha\beta} \\ \\ T''_{\alpha\beta} \end{pmatrix} \tag{19.46}$$

Obviously, probes should be selected so that $\mathbf{s}'_\pi\left(\hat{\mathbf{k}}\right) \times \mathbf{s}''_\pi\left(\hat{\mathbf{k}}\right) \neq \mathbf{0}$. If the first probe is linearly polarized, a "second" probe may be realized by rotating the first probe by 90° about its z axis.

In the most general setting, the Kerns transmission formula may be written

$$\frac{w'}{a_0} = \int_{-\infty}^{\infty}\int_{-\infty}^{\infty} \mathbf{s}'(\hat{\mathbf{k}}) \cdot \mathbf{t}(\hat{\mathbf{k}}) \frac{d\alpha\, d\beta}{\gamma k} \tag{19.47}$$

This describes the coupling between two arbitrarily positioned antennas, provided they can be separated by a planar surface (which is used to define the z direction). From this point of view, both the spherical and cylindrical transmission formulas may be considered special cases.

19.2.4 Spherical Scanning

19.2.4.1 Spherical Wave Representation Scalar solutions of Eq. (19.6), separated in spherical coordinates (Figure 19.3), are given by spherical waves

$$\begin{aligned} u_{nm}(\mathbf{r}) &= f_n(kr) Y_{nm}(\hat{\mathbf{r}}) \\ f_n(x) &= i^n h_n^{(1)}(x) \end{aligned} \tag{19.48}$$

(See Ref. 35, for example). Here, the $h_n^{(1)}$ are spherical Hankel functions of the first kind and the Y_{nm} are (scalar) spherical harmonics. The multipole index is a nonnegative integer, $n = 0, 1, \ldots$. For a given n, the azimuthal (or component) index is an integer m

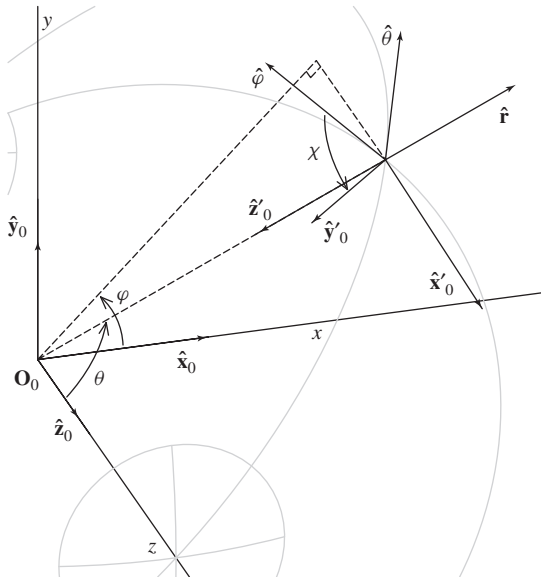

Figure 19.3 Spherical scanning geometry. The scan sphere is $r = d$. The test antenna is in its reference position (see Figure 19.1). The probe is shown at the position $(r, \varphi, \theta, \chi)$ with $r = d$, $\varphi = \pi/4$, and $\theta = \pi/3$. Furthermore, $\hat{\mathbf{y}}'_0 = \hat{\boldsymbol{\varphi}}$ when $\chi = 0$, $\hat{\mathbf{y}}'_0 = \hat{\boldsymbol{\theta}}$ when $\chi = -\pi/2$, and $\mathbf{z}'_0 = -\hat{\mathbf{r}}$.

in the range $-n \le m \le n$. (The nth multipole has $2n+1$ components.) Scalar spherical waves satisfy the radiation condition

$$u_{nm}(\mathbf{r}) \underset{r\to\infty}{\sim} Y_{nm}(\hat{\mathbf{r}}) \frac{\exp(ikr)}{ikr} \tag{19.49}$$

and the functions $u_{nm}(\mathbf{r})$ form a complete basis for representing fields in free space outside the minimum sphere $r = r_0$ that contains the sources. The plane wave representation

$$\begin{aligned} u_{nm}(\mathbf{r}) &= \int_{-\infty}^{\infty}\int_{-\infty}^{\infty} Y_{nm}\left(\hat{\mathbf{k}}\right) u_{\alpha\beta}(\mathbf{r}) \frac{d\alpha\, d\beta}{\gamma k} \\ &= \frac{1}{2\pi}\int_{-\infty}^{\infty}\int_{-\infty}^{\infty} Y_{nm}\left(\hat{\mathbf{k}}\right) \exp(i\mathbf{k}\cdot\mathbf{r}) \frac{d\alpha\, d\beta}{\gamma k}, \quad z > 0 \end{aligned} \tag{19.50}$$

can be established rigorously. See Eq. (19.24).

Vector solutions of Eqs. (19.4) and (19.6) follow directly from the scalar solutions (Eq. (19.48)):

$$\begin{aligned} \mathbf{m}_{nm}(\mathbf{r}) &= \frac{1}{k}\nabla \times \mathbf{n}_{nm}(\mathbf{r}) = \frac{1}{\sqrt{n(n+1)}}\mathbf{L}u_{nm}(\mathbf{r}) \\ \mathbf{n}_{nm}(\mathbf{r}) &= \frac{1}{k}\nabla \times \mathbf{m}_{nm}(\mathbf{r}) \end{aligned} \tag{19.51}$$

where the differential operator $\mathbf{L}$ is

$$\mathbf{L} = \frac{1}{i}\mathbf{r}\times\nabla = \frac{i}{\sin\theta}\hat{\boldsymbol{\theta}}\partial_\varphi - i\hat{\boldsymbol{\varphi}}\partial_\theta = \frac{i}{\sin\theta}\partial_\varphi\hat{\boldsymbol{\theta}} - \frac{i}{\sin\theta}\partial_\theta \sin\theta\hat{\boldsymbol{\varphi}} \tag{19.52}$$

That $\mathbf{m}_{nm}$ and $\mathbf{n}_{nm}$ are solutions of Eq. (19.6) is a consequence of the commutation relationships $\nabla^2\mathbf{L} = \mathbf{L}\nabla^2$ and $\nabla^2\nabla = \nabla\nabla^2$. Written out more fully,

$$\begin{aligned} \mathbf{m}_{nm}(\mathbf{r}) &= f_n(kr)\mathbf{X}^1_{nm}(\hat{\mathbf{r}}) \\ \mathbf{n}_{nm}(\mathbf{r}) &= g_n(kr)\mathbf{X}^2_{nm}(\hat{\mathbf{r}}) - \frac{\sqrt{n(n+1)}}{ikr} f_n(kr)\mathbf{X}^0_{nm}(\hat{\mathbf{r}}) \end{aligned} \tag{19.53}$$

with

$$\begin{aligned} f_n(x) &= i^n h_n(x) \underset{x\to\infty}{\sim} \frac{\exp(ix)}{ix} \\ g_n(x) &= \left[\frac{1}{ix}\frac{d}{dx}(xf_n)\right](x) \underset{x\to\infty}{\sim} \frac{\exp(ix)}{ix} \end{aligned} \tag{19.54}$$

The (vector) spherical harmonics [36, Chap. 9]

$$\begin{aligned} \mathbf{X}^0_{nm}(\hat{\mathbf{r}}) &= \hat{\mathbf{r}}Y_{nm}(\hat{\mathbf{r}}) \\ \mathbf{X}^1_{nm}(\hat{\mathbf{r}}) &= \frac{1}{\sqrt{n(n+1)}}\mathbf{L}Y_{nm}(\hat{\mathbf{r}}) = -\left(\hat{\boldsymbol{\theta}}\frac{m}{\sin\theta} + i\hat{\boldsymbol{\varphi}}\partial_\theta\right)\frac{Y_{nm}(\hat{\mathbf{r}})}{\sqrt{n(n+1)}} \\ \mathbf{X}^2_{nm}(\hat{\mathbf{r}}) &= i\hat{\mathbf{r}}\times\mathbf{X}^1_{nm}(\hat{\mathbf{r}}) \end{aligned} \tag{19.55}$$

form an orthonormal set

$$\int_0^{2\pi}\int_0^{\pi} \mathbf{X}_{\nu\mu}^{a*}(\hat{\mathbf{r}}) \cdot \mathbf{X}_{nm}^{b}(\hat{\mathbf{r}}) \sin\theta \, d\theta \, d\varphi = \delta_{ab}\delta_{\nu n}\delta_{\mu m} \tag{19.56}$$

We have the asymptotic formulas

$$\begin{aligned} \mathbf{m}_{nm}(\mathbf{r}) &\underset{r\to\infty}{\sim} \mathbf{X}_{nm}^{1}(\hat{\mathbf{r}}) \frac{\exp(ikr)}{ikr} \\ \mathbf{n}_{nm}(\mathbf{r}) &\underset{r\to\infty}{\sim} \mathbf{X}_{nm}^{2}(\hat{\mathbf{r}}) \frac{\exp(ikr)}{ikr} \end{aligned} \tag{19.57}$$

and the corresponding plane wave representations

$$\begin{aligned} \mathbf{m}_{nm}(\mathbf{r}) &= \frac{1}{2\pi}\int_{-\infty}^{\infty}\int_{-\infty}^{\infty} \mathbf{X}_{nm}^{1}(\hat{\mathbf{k}}) \exp(i\mathbf{k}\cdot\mathbf{r}) \frac{d\alpha \, d\beta}{\gamma k} \\ \mathbf{n}_{nm}(\mathbf{r}) &= \frac{1}{2\pi}\int_{-\infty}^{\infty}\int_{-\infty}^{\infty} \mathbf{X}_{nm}^{2}(\hat{\mathbf{k}}) \exp(i\mathbf{k}\cdot\mathbf{r}) \frac{d\alpha \, d\beta}{\gamma k}, \quad z > 0 \end{aligned} \tag{19.58}$$

The electromagnetic fields of a test antenna (in the reference position) can be written as the superposition

$$\begin{aligned} \mathbf{E}(\mathbf{r}) &= a_0 \sum_{n=1}^{\infty}\sum_{m=-n}^{n} \left[t_{nm}^{1}\mathbf{m}_{nm}(\mathbf{r}) + t_{nm}^{2}\mathbf{n}_{nm}(\mathbf{r}) \right] \\ iZ_0\mathbf{H}(\mathbf{r}) &= a_0 \sum_{n=1}^{\infty}\sum_{m=-n}^{n} \left[t_{nm}^{2}\mathbf{m}_{nm}(\mathbf{r}) + t_{nm}^{1}\mathbf{n}_{nm}(\mathbf{r}) \right], \quad r > r_0 \end{aligned} \tag{19.59}$$

There is no monopole term ($n = 0$) in spherical wave expansions of the electromagnetic fields in free space. Using Eq. (19.57), we obtain the asymptotic formula

$$\mathbf{E}(\mathbf{r}) \underset{r\to\infty}{\sim} a_0 \mathbf{t}_0(\hat{\mathbf{r}}) \frac{\exp(ikr)}{ikr}$$

where the transmitting function is

$$\mathbf{t}_0(\hat{\mathbf{r}}) = \sum_{n=1}^{\infty}\sum_{m=-n}^{n} \left[t_{nm}^{1}\mathbf{X}_{nm}^{1}(\hat{\mathbf{r}}) + t_{nm}^{2}\mathbf{X}_{nm}^{2}(\hat{\mathbf{r}}) \right] \tag{19.60}$$

From Eq. (19.59),

$$\begin{aligned} \mathbf{E}_t(\mathbf{r}) &= \mathbf{E}(\mathbf{r}) - \hat{\mathbf{r}}\hat{\mathbf{r}} \cdot \mathbf{E}(\mathbf{r}) \\ &= a_0 \sum_{n=1}^{\infty}\sum_{m=-n}^{n} \left[f_n(kr) \, t_{nm}^{1}\mathbf{X}_{nm}^{1}(\mathbf{r}) + g_n(kr) \, t_{nm}^{2}\mathbf{X}_{nm}^{2}(\mathbf{r}) \right] \end{aligned} \tag{19.61}$$

An application of the orthogonalities in Eq. (19.56) yields

$$t_{nm}^{1} = \frac{1}{f_n(kr)} \int_0^{2\pi} \int_0^{\pi} \mathbf{X}_{nm}^{1*}(\hat{\mathbf{r}}) \cdot \frac{\mathbf{E}(\mathbf{r})}{a_0} \sin\theta \, d\theta \, d\varphi$$
$$t_{nm}^{2} = \frac{1}{g_n(kr)} \int_0^{2\pi} \int_0^{\pi} \mathbf{X}_{nm}^{2*}(\hat{\mathbf{r}}) \cdot \frac{\mathbf{E}(\mathbf{r})}{a_0} \sin\theta \, d\theta \, d\varphi, \quad r = d > r_0 \tag{19.62}$$

Thus the transmitting pattern is determined by the tangential electric field on any sphere $r = d > r_0$.

19.2.4.2 Probe Response We begin with the test antenna and probe in their reference positions. In spherical scanning, the response of the probe is recorded as the probe is rotated over a measurement sphere of radius $r = r' = d$. First the probe is rotated by angle $\chi = \chi'$ about the laboratory z axis. Then it is rotated by angle $\theta = \theta'$ about the laboratory y axis. Finally, the probe is again rotated about the laboratory z axis by an angle $\varphi = \varphi'$. The members of the triplet (φ, θ, χ) are collectively known as *Euler angles*.† (The positive sense of these angles is determined, in the usual manner, with the "right-hand rule.") The angles φ' and θ' fix the location of the probe on the measurement sphere. The angle χ' specifies a rotation about the probe axis. When $\chi' = 0$, $\hat{\mathbf{y}}_0' = \hat{\boldsymbol{\varphi}}$, and when $\chi' = -\pi/2$, $\hat{\mathbf{y}}_0' = \hat{\boldsymbol{\theta}}$. See Figure 19.3.

In the laboratory coordinate system, position (location and orientation) of the probe is described by the parameter set $(r, \varphi, \theta, \chi)$ with the probe reference position corresponding to $(d, 0, 0, 0)$. The position of a similarly rotated test antenna is also described by these parameters with the test antenna reference position corresponding to $(0, 0, 0, 0)$.

Consider the output when the test antenna is at its reference position and the probe is at $\left(r', \varphi', \theta', \chi'\right)$. The same output will be observed when the probe is at its reference position and the test antenna is at $\left(0, -\chi', -\theta', -\varphi', \right)$. This fact may be expressed mathematically as

$$w'\left(r', \varphi', \theta', \chi'\right) = \left[\mathcal{P} \cdot \mathbf{E}\right]\left(r', \varphi', \theta', \chi', \right) = \left[\mathcal{P} \cdot \tilde{\mathbf{E}}\right]\left(r', 0, 0, 0\right) \tag{19.63}$$

Here $\mathcal{P}$ is a linear operator that represents the probe, $\mathbf{E}(\mathbf{r})$ is the electric field of the test antenna (at its reference position), and $\tilde{\mathbf{E}}(\mathbf{r})$ is the field of the rotated test antenna.

Now, let the "test antenna" radiate the vector spherical wave $\mathbf{m}_{nm}(\mathbf{r})$ or $\mathbf{n}_{nm}(\mathbf{r})$. As it turns out, rotated n-poles can be reexpressed as superpositions of multipole components with the same multipole index n:

$$\tilde{\mathbf{m}}_{nm}(\mathbf{r}) = \sum_{\mu=-n}^{n} \mathbf{m}_{n\mu}(\mathbf{r}) D_{\mu m}^{n}(-\chi', -\theta', -\varphi')$$
$$\tilde{\mathbf{n}}_{nm}(\mathbf{r}) = \sum_{\mu=-n}^{n} \mathbf{n}_{n\mu}(\mathbf{r}) D_{\mu m}^{n}(-\chi', -\theta', -\varphi') \tag{19.64}$$

†The reader should be aware that several definitions of Euler angles are commonly used.

We apply the Euler angles as rotations about axes fixed in the laboratory coordinate system. An equivalent result may be obtained by rotating about axes fixed in the body being moved. Begin with the laboratory and body coordinate systems coincident: first rotate by angle φ about the body z axis; then rotate by angle θ about the body y axis; finally, rotate by angle χ about the body z axis.

We discuss the rotation functions $D^n_{\mu m}$ later. From Eqs. (19.63) and (19.64)

$$w^{1\prime}_{nm}\left(r', \varphi', \theta', \chi'\right) = \left[\boldsymbol{\mathcal{P}} \cdot \tilde{\mathbf{m}}_{nm}\right]\left(r', 0, 0, 0\right) = \sum_{\mu=-n}^{n} \sigma^{1\prime}_{n\mu}(r') D^n_{\mu m}(-\chi', -\theta', -\varphi')$$

$$w^{2\prime}_{nm}\left(r', \varphi', \theta', \chi'\right) = \left[\boldsymbol{\mathcal{P}} \cdot \tilde{\mathbf{n}}_{nm}\right]\left(r', 0, 0, 0\right) = \sum_{\mu=-n}^{n} \sigma^{2\prime}_{n\mu}(r') D^n_{\mu m}(-\chi', -\theta', -\varphi') \tag{19.65}$$

The translated probe coefficients are

$$\begin{aligned} \sigma^{1\prime}_{n\mu}(r) &= \left[\boldsymbol{\mathcal{P}} \cdot \mathbf{m}_{n\mu}\right](r, 0, 0, 0) \\ \sigma^{2\prime}_{n\mu}(r) &= \left[\boldsymbol{\mathcal{P}} \cdot \mathbf{n}_{n\mu}\right](r, 0, 0, 0) \end{aligned} \tag{19.66}$$

Thus the response of the probe to the modes $\mathbf{m}_{nm}(\mathbf{r})$ or $\mathbf{n}_{nm}(\mathbf{r})$ can be summarized in terms of the $2n + 1$ numbers $\sigma^{1\prime}_{n\mu}$ or $\sigma^{2\prime}_{n\mu}$ that are the responses of the probe, in its reference position, to the n-pole component functions.

Appendix C.2 discusses the evaluation of the translated probe coefficients (Eq. (19.66)), which depend on the known receiving function of the probe.

19.2.4.3 Jensen Transmission Equation In Eq. (19.59) we have a modal expansion corresponding to Eq. (19.1). In Eq. (19.65) we have the response of the probe to each mode corresponding to Eq. (19.2). Finally, corresponding to Eq. (19.3), we have the *Jensen transmission formula* [6]

$$\frac{w'(r, \varphi, \theta, \chi)}{a_0} = \sum_{n=1}^{\infty} \sum_{m=-n}^{n} \sum_{\mu=-n}^{n} \left[\sigma^{1\prime}_{n\mu}(r) t^1_{nm} + \sigma^{2\prime}_{n\mu}(r) t^2_{nm}\right] D^n_{\mu m}(-\chi, -\theta, -\varphi) \tag{19.67}$$

A full discussion of the rotation functions[†]

$$D^n_{\mu m}(-\chi, -\theta, -\varphi) = \exp(i\mu\chi) d^n_{\mu m}(-\theta) \exp(im\varphi) \tag{19.68}$$

is beyond the scope of this chapter. The orthogonalities of the $D^n_{\mu m}$ can be used to solve for the unknown $t^{1,2}_{nm}$. In particular, were the translated probe coefficients $\sigma^{1\prime}_{n\mu}$ and $\sigma^{2\prime}_{n\mu}$ significant for $|\mu| \leq N_p$, then measurements would be required at $2N_P + 1$ values of χ for each (φ, θ). In order to require only two spin values per direction and to retain the advantages of orthogonality, standard practice employs special probes [26] designed so that $\sigma^{1\prime}_{n\mu} = \sigma^{2\prime}_{n\mu} = 0$ unless $\mu = \pm 1$.

Consider such a $\mu = \pm 1$ *probe* and define the *measurement vector*

$$\mathbf{w}'(\mathbf{r}) = w'_\theta(r, \varphi, \theta)\hat{\boldsymbol{\theta}} + w'_\varphi(r, \varphi, \theta)\hat{\boldsymbol{\varphi}} \tag{19.69}$$

[†]We define the rotation functions according to the convention of Rose [37] and Tinkham [38]. To use the convention of Edmonds [39], substitute $D^n_{\mu m}(\varphi, \theta, \chi)$ for $D^n_{\mu m}(-\chi, -\theta, -\varphi)$. To use the convention of Hansen [26], substitute $D^n_{\mu m}(\chi, \theta, \varphi)$ for $D^n_{\mu m}(-\chi, -\theta, -\varphi)$.

$$\begin{aligned} w'_{\varphi}(r,\varphi,\theta) &= w'(r,\varphi,\theta,\chi=0) \\ w'_{\theta}(r,\varphi,\theta) &= w'(r,\varphi,\theta,\chi=-\pi/2) \end{aligned} \tag{19.70}$$

With

$$d^{n}_{\pm 1,m}(-\theta)\exp(im\varphi) = \sqrt{\frac{4\pi}{2n+1}}\left(\hat{\boldsymbol{\theta}} \mp i\hat{\boldsymbol{\varphi}}\right)\cdot \mathbf{X}^{1}_{nm}(\hat{\mathbf{r}}) \tag{19.71}$$

the Jensen transmission formula Eq. (19.67) can be written [23, Eq. (27)]

$$\frac{\mathbf{w}'(\mathbf{r})}{a_0} = \sum_{n=1}^{\infty}\sum_{m=-n}^{n}\left[T^{1\prime}_{nm}(r)\,\mathbf{X}^{1}_{nm}(\hat{\mathbf{r}}) + T^{2\prime}_{nm}(r)\,\mathbf{X}^{2}_{nm}(\hat{\mathbf{r}})\right] \tag{19.72}$$

where in matrix form

$$\begin{pmatrix} T^{1\prime}_{nm} \\ \\ T^{2\prime}_{nm} \end{pmatrix} = -i\sqrt{\frac{4\pi}{2n+1}}\begin{pmatrix} \sigma^{1\prime}_{n1} - \sigma^{1\prime}_{n,-1} & \sigma^{2\prime}_{n1} - \sigma^{2\prime}_{n,-1} \\ \\ \sigma^{1\prime}_{n1} + \sigma^{1\prime}_{n,-1} & \sigma^{2\prime}_{n1} + \sigma^{2\prime}_{n,-1} \end{pmatrix}\begin{pmatrix} t^{1}_{nm} \\ \\ t^{2}_{nm} \end{pmatrix} \tag{19.73}$$

Equations (19.67) and (19.72) are valid when multiple reflections can be ignored and when the probe and test antenna can be physically separated by a plane perpendicular to $\hat{\mathbf{r}}$.

Application of the orthogonalities in Eq. (19.56) gives

$$\begin{aligned} T^{1\prime}_{nm} &= \int_0^{2\pi}\int_0^{\pi}\mathbf{X}^{1*}_{nm}(\hat{\mathbf{r}})\cdot\frac{\mathbf{w}'(\mathbf{r})}{a_0}\sin\theta\,d\theta\,d\varphi \\ T^{2\prime}_{nm} &= \int_0^{2\pi}\int_0^{\pi}\mathbf{X}^{2*}_{nm}(\hat{\mathbf{r}})\cdot\frac{\mathbf{w}'(\mathbf{r})}{a_0}\sin\theta\,d\theta\,d\varphi, \quad r=d \end{aligned} \tag{19.74}$$

Finally, Eq. (19.73) provides two equations that can be solved for t^{1}_{nm} and t^{2}_{nm}:

$$\begin{pmatrix} t^{1}_{nm} \\ \\ t^{2}_{nm} \end{pmatrix} = \frac{i\sqrt{\dfrac{2n+1}{16\pi}}}{\sigma^{1\prime}_{n1}\sigma^{2\prime}_{n,-1} - \sigma^{1\prime}_{n,-1}\sigma^{2\prime}_{n1}}\begin{pmatrix} \sigma^{2\prime}_{n1} + \sigma^{2\prime}_{n,-1} & -\sigma^{2\prime}_{n1} + \sigma^{2\prime}_{n,-1} \\ \\ -\sigma^{1\prime}_{n1} - \sigma^{1\prime}_{n,-1} & \sigma^{1\prime}_{n1} - \sigma^{1\prime}_{n,-1} \end{pmatrix}\begin{pmatrix} T^{1\prime}_{nm} \\ \\ T^{2\prime}_{nm} \end{pmatrix} \tag{19.75}$$

Thus the transmitting function is determined by data $\mathbf{w}'(\mathbf{r})/a_0$ measured on the sphere $r = d$. Unlike planar and cylindrical scanning, where the second probe may be distinct, the present formulation of spherical scanning assumes that one probe is used in two orientations. If this probe is circularly polarized, then Eqs. (19.73) will not be independent; however, if a complete set of measurement data is obtained for both a right- and a left-circularly polarized probe, then the resulting set of four equations can be solved for t^{1}_{nm} and t^{2}_{nm} in a least-squares sense.

An example $\mu = \pm 1$ probe is the conceptual *ideal probe* that directly measures a component of the transverse electric field; however, physical $\mu = \pm 1$ probes are not difficult to construct (see Appendix A.2). In fact, any practical probe will approach a $\mu = \pm 1$ probe as the separation between test antenna and probe increases.

Formula (19.71) can be derived from first principles by forcing Eqs. (19.61) and (19.67) to agree when the probe is ideal.

19.2.5 Cylindrical Scanning

19.2.5.1 Cylindrical Wave Representation Scalar solutions of Eq. (19.6), separated in cylindrical coordinates (Figure 19.4), are given by the cylindrical waves

$$u_{n\beta}(\mathbf{r}) = \frac{1}{\sqrt{2\pi}} F_n(\kappa\rho)\, \Psi_n(\hat{\boldsymbol{\rho}}) \exp(i\beta y) \tag{19.76}$$

$$F_n(x) = i^n \sqrt{\frac{\pi}{2}} H_n^{(1)}(x)$$

$$\Psi_n(\hat{\boldsymbol{\rho}}) = \frac{1}{\sqrt{2\pi}} \left(\frac{z + ix}{\rho}\right)^n = \frac{\exp(in\Phi)}{\sqrt{2\pi}} \tag{19.77}$$

Here, the $H_n^{(1)}$ are cylindrical Hankel functions of the first kind [40, Chap. 9] and

$$\begin{aligned} \rho &= \sqrt{r^2 - y^2} \\ \kappa &= \sqrt{k^2 - \beta^2} \\ \hat{\boldsymbol{\rho}} &= \frac{z\hat{\mathbf{z}} + x\hat{\mathbf{x}}}{\rho} \end{aligned} \tag{19.78}$$

In order to keep the reference positions of the test antenna and the probe on the z axis, we take the y axis as the axis of cylinders of constant ρ. Cylindrical waves propagate or decay away from the y axis when κ is real ($k > \beta$) or imaginary ($k < \beta$), respectively. If sources are confined to the region $\rho < \rho_0$, then the functions $u_{n\beta}$ form a complete basis for representing fields in free space $\rho > \rho_0$. The plane wave decomposition

$$\begin{aligned} u_{n\beta}(\mathbf{r}) &= \int_{-\infty}^{\infty} \Psi_n(\hat{\boldsymbol{\kappa}}) u_{\alpha\beta}(\mathbf{r}) \frac{d\alpha}{\gamma} \\ &= \frac{1}{2\pi} \int_{-\infty}^{\infty} \Psi_n(\hat{\boldsymbol{\kappa}}) \exp(i\mathbf{k}\cdot\mathbf{r}) \frac{d\alpha}{\gamma}, \quad z > 0 \end{aligned} \tag{19.79}$$

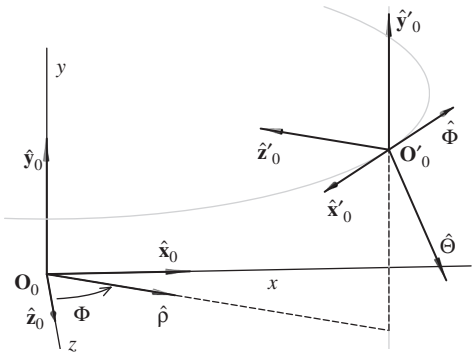

Figure 19.4 Cylindrical scanning geometry. The scan cylinder is $\rho = d$. The test antenna is in its reference position (see Figure 19.1). The probe is shown at the position (ρ, Φ, y) with $\rho = d$, $\Phi = \pi/3$, and $y = d/2$. Furthermore, $\hat{\mathbf{x}}'_0 = -\hat{\boldsymbol{\Phi}}$, $\hat{\mathbf{y}}'_0 = \hat{\mathbf{y}}$, $\hat{\mathbf{z}}'_0 = -\hat{\boldsymbol{\rho}}$, and $\hat{\boldsymbol{\Theta}} = \hat{\boldsymbol{\Phi}} \times \hat{\mathbf{r}}$.

where

$$\hat{\boldsymbol{\kappa}} = \frac{\gamma\hat{\mathbf{z}} + \alpha\hat{\mathbf{x}}}{\kappa} \tag{19.80}$$

can be established rigorously [41, Eqs. (3.753) and (3.754)]. See Eq. (19.24).

Vector solutions of Eqs. (19.4) and (19.6) follow directly from the scalar solutions of Eq. (19.76):

$$\begin{aligned}\mathbf{m}_{n\beta}(\mathbf{r}) &= \frac{1}{k}\nabla \times \mathbf{n}_{n\beta}(\mathbf{r}) = \frac{1}{i\kappa}\hat{\mathbf{y}} \times \nabla u_{n\beta} \\ &= \frac{1}{\sqrt{2\pi}}\left[-\frac{nF_n(\kappa\rho)}{\kappa\rho}\hat{\boldsymbol{\rho}} + G_n(\kappa\rho)\hat{\boldsymbol{\Phi}}\right]\Psi_n(\hat{\boldsymbol{\rho}})\exp(i\beta y)\end{aligned} \tag{19.81}$$

$$\begin{aligned}\mathbf{n}_{n\beta}(\mathbf{r}) &= \frac{1}{k}\nabla \times \mathbf{m}_{n\beta}(\mathbf{r}) = -\frac{\beta}{ik}\hat{\mathbf{y}} \times \mathbf{m}_{n\beta}(\mathbf{r}) - \frac{\kappa}{ik}u_{n\beta}(\mathbf{r})\hat{\mathbf{y}} \\ &= \frac{1}{\sqrt{2\pi}}\left[\frac{\beta}{ik}G_n(\kappa\rho)\hat{\boldsymbol{\rho}} + \frac{\beta}{ik}\frac{nF_n(\kappa\rho)}{\kappa\rho}\hat{\boldsymbol{\Phi}} - \frac{\kappa}{ik}F_n(\kappa\rho)\,\hat{\mathbf{y}}\right]\Psi_n(\hat{\boldsymbol{\rho}})\exp(i\beta y)\end{aligned} \tag{19.82}$$

with

$$\begin{aligned}F_n(x) &= i^n\sqrt{\frac{\pi}{2}}H_n^{(1)}(x) \underset{x\to\infty}{\sim} \frac{\exp(ix)}{\sqrt{ix}} \\ G_n(x) &= \frac{1}{i}\frac{d}{dx}F_n(x) \underset{x\to\infty}{\sim} \frac{\exp(ix)}{\sqrt{ix}}\end{aligned} \tag{19.83}$$

From Eqs. (19.79), (19.81), and (19.82), we have the plane wave decompositions

$$\begin{aligned}\mathbf{m}_{n\beta}(\mathbf{r}) &= \frac{1}{2\pi}\int_{-\infty}^{\infty}\boldsymbol{\Psi}_n^1(\hat{\mathbf{k}})\exp(i\mathbf{k}\cdot\mathbf{r})\frac{d\alpha}{\gamma} \\ \mathbf{n}_{n\beta}(\mathbf{r}) &= \frac{1}{2\pi}\int_{-\infty}^{\infty}\boldsymbol{\Psi}_n^2(\hat{\mathbf{k}})\exp(i\mathbf{k}\cdot\mathbf{r})\frac{d\alpha}{\gamma}, \quad z > 0\end{aligned} \tag{19.84}$$

The angular functions are

$$\begin{aligned}\boldsymbol{\Psi}_n^1(\hat{\mathbf{r}}) &= \hat{\mathbf{y}} \times \hat{\boldsymbol{\rho}}\Psi_n(\hat{\boldsymbol{\rho}}) = \Psi_n(\hat{\boldsymbol{\rho}})\hat{\boldsymbol{\Phi}} \\ \boldsymbol{\Psi}_n^2(\hat{\mathbf{r}}) &= i\hat{\mathbf{r}} \times \boldsymbol{\Psi}_n^1(\hat{\boldsymbol{\rho}}) = -i\Psi_n(\hat{\boldsymbol{\rho}})\hat{\boldsymbol{\Theta}}\end{aligned} \tag{19.85}$$

The electromagnetic fields of a test antenna (in the reference position) can be written as the superposition

$$\begin{aligned}\mathbf{E}(\mathbf{r}) &= a_0\sum_{n=-\infty}^{\infty}\int_{-\infty}^{\infty}\left[t_{n\beta}^1\mathbf{m}_{n\beta}(\mathbf{r}) + t_{n\beta}^2\mathbf{n}_{n\beta}(\mathbf{r})\right]\frac{d\beta}{k} \\ iZ_0\mathbf{H}(\mathbf{r}) &= a_0\sum_{n=-\infty}^{\infty}\int_{-\infty}^{\infty}\left[t_{n\beta}^2\mathbf{m}_{n\beta}(\mathbf{r}) + t_{n\beta}^1\mathbf{n}_{n\beta}(\mathbf{r})\right]\frac{d\beta}{k}, \quad \rho > \rho_0\end{aligned} \tag{19.86}$$

A substitution of Eq. (19.84) yields the plane wave expansion

$$\mathbf{E}(\mathbf{r}) = \frac{a_0}{2\pi}\int_{-\infty}^{\infty}\int_{-\infty}^{\infty}\mathbf{t}_0(\hat{\mathbf{k}})\exp(i\mathbf{k}\cdot\mathbf{r})\frac{d\alpha\, d\beta}{\gamma k}, \quad z > \rho_0$$

where the transmitting function is represented by the Fourier series

$$\mathbf{t}_0(\hat{\mathbf{r}}) = \sum_{n=-\infty}^{\infty}\left[t^1_{n,ky/r}\boldsymbol{\Psi}^1_n(\hat{\mathbf{r}}) + t^2_{n,ky/r}\boldsymbol{\Psi}^2_n(\hat{\mathbf{r}})\right] \tag{19.87}$$

By inverting the Fourier transform and applying the orthogonality

$$\int_0^{2\pi}\Psi^*_\nu(\hat{\boldsymbol{\rho}})\Psi_n(\hat{\boldsymbol{\rho}})d\Phi = \delta_{\nu n} \tag{19.88}$$

we can solve Eq. (19.86) for the cylindrical-mode coefficients

$$\begin{aligned} t^1_{n\beta} &= \frac{1}{G_n(\kappa\rho)}\frac{k}{2\pi}\int_0^{2\pi}\int_{-\infty}^{\infty}\left(\hat{\boldsymbol{\Phi}} + \frac{n\beta}{\kappa^2\rho}\hat{\mathbf{y}}\right)\cdot\frac{\mathbf{E}(\mathbf{r})}{a_0}\exp(-in\Phi - i\beta y)\,dy\,d\Phi \\ t^2_{n\beta} &= \frac{1}{F_n(\kappa\rho)}\frac{k}{2\pi}\int_0^{2\pi}\int_{-\infty}^{\infty}\frac{k}{i\kappa}\hat{\mathbf{y}}\cdot\frac{\mathbf{E}(\mathbf{r})}{a_0}\exp\left(-in\Phi - i\beta y\right)\,dy\,d\Phi, \quad \rho = d > \rho_0 \end{aligned} \tag{19.89}$$

Thus the transmitting function is determined by the tangential electric field on any cylinder $\rho = d > \rho_0$.

19.2.5.2 Probe Response We begin with the test antenna and probe in their reference positions. In cylindrical scanning, the response of the probe is recorded as the probe is translated and rotated over a measurement cylinder of radius $\rho = \rho' = d$. The probe is translated in the $\hat{\mathbf{y}}$ direction by a distance $y = y'$. Then the probe is rotated about the y axis by an angle $\Phi = \Phi'$. (The positive sense of Φ is determined, in the usual manner, with the "right-hand rule.") See Figure 19.4.

In the laboratory coordinate system, position (location and orientation) of the probe is described by the parameter set (ρ, Φ, y) with the probe reference position corresponding to $(d, 0, 0)$. The position of a similarly rotated and translated test antenna is also described by these parameters with the test antenna reference position corresponding to $(0, 0, 0)$.

Consider the output with the test antenna at its reference position and the probe at $\left(\rho', \Phi', y'\right)$. The same output will be observed with the probe at its reference position and the test antenna at $\left(0, -\Phi', -y'\right)$. This fact may be expressed mathematically as

$$w'\left(\mathbf{r}'\right) = \left[\boldsymbol{\mathcal{P}}\cdot\mathbf{E}\right]\left(\rho', \Phi', y'\right) = \left[\boldsymbol{\mathcal{P}}\cdot\tilde{\mathbf{E}}\right]\left(\rho', 0, 0\right) \tag{19.90}$$

Here $\boldsymbol{\mathcal{P}}$ is a linear operator that represents the probe, $\mathbf{E}(\mathbf{r})$ is the field of the test antenna (at its reference position), and $\tilde{\mathbf{E}}(\mathbf{r})$ is the field of the rotated and translated test antenna.

Now, let the "test antenna" radiate the vector cylindrical wave $\mathbf{m}_{n\beta}$ or $\mathbf{n}_{n\beta}$. Then,

$$\begin{aligned} \tilde{\mathbf{m}}_{n\beta}(\mathbf{r}) &= \mathbf{m}_{n\beta}(\rho, \Phi + \Phi', y + y') = \mathbf{m}_{n\beta}(\mathbf{r})\exp(in\Phi' + i\beta y') \\ \tilde{\mathbf{n}}_{n\beta}(\mathbf{r}) &= \mathbf{n}_{n\beta}(\rho, \Phi + \Phi', y + y') = \mathbf{n}_{n\beta}(\mathbf{r})\exp(in\Phi' + i\beta y') \end{aligned} \tag{19.91}$$

From Eqs. (19.90) and (19.91),

$$\begin{aligned} w_{n\beta}^{1'}(\mathbf{r}') &= \left[\boldsymbol{\mathcal{P}} \cdot \tilde{\mathbf{m}}_{n\beta}\right](\rho', 0, 0) = \sigma_{n\beta}^{1'}(\rho') \exp(in\Phi' + i\beta y') \\ w_{n\beta}^{2'}(\mathbf{r}') &= \left[\boldsymbol{\mathcal{P}} \cdot \tilde{\mathbf{n}}_{n\beta}\right](\rho', 0, 0) = \sigma_{n\beta}^{2'}(\rho') \exp(in\Phi' + i\beta y') \end{aligned} \tag{19.92}$$

The translated probe coefficients are

$$\begin{aligned} \sigma_{n\beta}^{1'}(\rho) &= \left[\boldsymbol{\mathcal{P}} \cdot \mathbf{m}_{n\beta}\right](\rho, 0, 0) \\ \sigma_{n\beta}^{2'}(\rho) &= \left[\boldsymbol{\mathcal{P}} \cdot \mathbf{n}_{n\beta}\right](\rho, 0, 0) \end{aligned} \tag{19.93}$$

Thus $w_{n\beta}^{1'}(\mathbf{r}')$ and $w_{n\beta}^{2'}(\mathbf{r}')$ depend on the transverse location of the probe through a simple phase factor.

Appendix C.3 discusses the evaluation of the translated probe coefficients in Eq. (19.93), which depend on the known receiving function of the probe.

19.2.5.3 Transmission Equation In Eq. (19.86) we have a modal expansion corresponding to Eq. (19.1). In Eq. (19.92) we have the response of the probe to each mode corresponding to Eq. (19.2). Finally, corresponding to Eq. (19.3), we have the transmission formula [10–12]

$$\frac{w'(\mathbf{r})}{a_0} = \sum_{n=-\infty}^{\infty} \int_{-\infty}^{\infty} \left[\sigma_{n\beta}^{1'}(\rho) t_{n\beta}^{1} + \sigma_{n\beta}^{2'}(\rho) t_{n\beta}^{2}\right] \exp(in\Phi + i\beta y) \frac{d\beta}{k} \tag{19.94}$$

(Brown and Jull [5] earlier developed a two-dimensional form of this equation.) Equation (19.94) is valid when multiple reflections can be ignored and when the probe and test antenna can be physically separated by a plane perpendicular to $\hat{\boldsymbol{\rho}}$.

Inversion of the Fourier transform and use of the orthogonality in Eq. (19.88) gives

$$\begin{aligned} T_{n\beta}'(\rho) &= \sigma_{n\beta}^{1'} t_{n\beta}^{1} + \sigma_{n\beta}^{2'} t_{n\beta}^{2} \\ &= \frac{k}{4\pi^2} \int_0^{2\pi} \int_{-\infty}^{\infty} \frac{w'(\mathbf{r})}{a_0} \exp(-in\Phi - i\beta y)\, dy\, d\Phi, \quad \rho = d \end{aligned} \tag{19.95}$$

Since $T_{n\beta}'$ can be computed from data $w'(\mathbf{r})/a_0$ measured on the cylinder $\rho = d$, Eq. (19.95) provides one equation for the two unknown components of $\mathbf{t}_0(\hat{\mathbf{k}})$. Data from a second probe are needed to provide sufficient information to solve for $\mathbf{t}_0(\hat{\mathbf{k}})$. With two probes, we have the linear system

$$\begin{pmatrix} T_{n\beta}' \\ \\ T_{n\beta}'' \end{pmatrix} = \begin{pmatrix} \sigma_{n\beta}^{1'} & \sigma_{n\beta}^{2'} \\ \\ \sigma_{n\beta}^{1''} & \sigma_{n\beta}^{2''} \end{pmatrix} \begin{pmatrix} t_{n\beta}^{1} \\ \\ t_{n\beta}^{1} \end{pmatrix} \tag{19.96}$$

Here, quantities associated with the second probe are marked with a double prime. Thus

$$\begin{pmatrix} t_{n\beta}^{1} \\ \\ t_{n\beta}^{1} \end{pmatrix} = \frac{1}{\sigma_{n\beta}^{1'}\sigma_{n\beta}^{2''} - \sigma_{n\beta}^{1''}\sigma_{n\beta}^{2'}} \begin{pmatrix} \sigma_{n\beta}^{2''} & -\sigma_{n\beta}^{2'} \\ \\ -\sigma_{n\beta}^{1''} & \sigma_{n\beta}^{1'} \end{pmatrix} \begin{pmatrix} T_{n\beta}' \\ \\ T_{n\beta}'' \end{pmatrix} \tag{19.97}$$

If the first probe is linearly polarized, then a "second" probe may be realized by rotating the first probe by 90° about its z axis.

19.3 NEAR-FIELD MEASUREMENT PRACTICE

19.3.1 General Considerations for Near-Field Scanning

19.3.1.1 Overview Here (Section 19.3.1) we discuss practical issues that are substantially the same for all implementations of near-field scanning methods. Later sections deal with geometry-specific considerations: planar scanning (Section 19.3.2), spherical scanning (Section 19.3.3), and cylindrical scanning (Section 19.3.4).

19.3.1.2 Implementation

RF Equipment Transformation from near field to far field requires complex data (both amplitude and phase information). Figure 19.5 shows a typical antenna measurement system. Key components include a phase/amplitude receiver and a phase-stable signal source, such as that provided by a synthesizer. Because cables may be long, remote mixing is often used to reduce attenuation.

Alignment Equipment Requirements and techniques vary from geometry to geometry, but the basic alignment tools are the same. These include laser straightness interferometers, electronic levels, and theodolites (with autocollimation capability). A laser tracker can greatly reduce the time required by and improve the accuracy of some procedures.

Probe Characterization To evaluate the far-field properties of the test antenna from near-field measurements, it is necessary to know the far-field properties of a reference antenna (probe). These properties (gain, polarization, and pattern) are usually measured with traditional far-field techniques, which are not in the scope of this chapter. See Refs. 42–44.

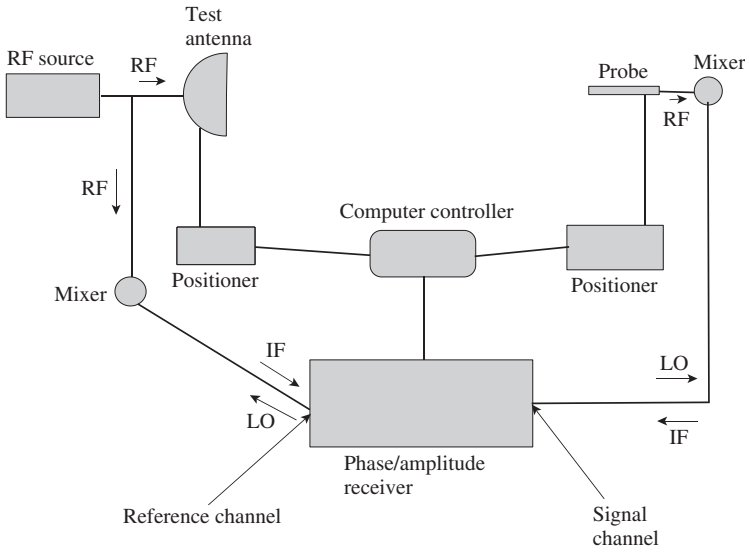

Figure 19.5 Typical components of a near-field measurement system.

Absorber and Absorber Placement The use of a good quality microwave absorber helps to reduce the effects of stray signals. As discussed previously, the planar technique is best used for moderately to highly directive antennas. Since the antenna under test (AUT) is fixed in the laboratory, it is usually sufficient to place absorber only in front of the test antenna. The mounting structure behind the probe is especially critical. More absorber coverage is needed for nondirective and/or rotating test antennas. For many cylindrical and spherical scanning implementations, a full anechoic chamber is required. Typically, a pyramidal absorber is used. The optimal size of the pyramids depends on the operational frequency range.

Microwave absorber (even that treated with fire retardant salts) is flammable [45]. Once ignited, absorber burns hot and produces many toxic gases, including cyanide, carbon monoxide, carbon dioxide, and hydrochloric acid. Potential ignition sources should be treated with care. These include high power RF radiation (beyond the rating of the absorber), soldering and welding irons, and high intensity lights.

Cross-Talk and Leakage Cross-talk is the unwanted coupling between two ports of a measurement system or subsystem. Examples include signals traveling from the reference channel to the measurement channel of the receiver; signals traveling from the x polarization port to the y polarization port of a dual-port probe; and signals traveling from the LO (local oscillator) port to the RF port of a remote mixer. A good receiver will have 80 dB or better of isolation between the reference and measurement channels. Cross-talk problems are often due to poor isolation in switches, mixers, isolators, or dual-port probes. The direct way to test for cross-talk is to insert a signal into one port and measure the output at the other port.

Leakage is unwanted coupling due to imperfections in the cables, connectors, and joints used to link the components of a measurement system. One technique of checking for leakage is to make three near-field scans: a reference scan is taken with the AUT transmitting and the probe receiving the signal; a second scan is taken with the transmit signal terminated at the antenna and a third is taken with the receive signal terminated. The second scan detects leakage in the circuit preceding the transmitting antenna The third scan detects leakage in the circuit following the receiving antenna. (See Figure 19.6.)

The bias is the average leakage signal over the scan area. A nonzero bias can lead to a spurious peak in the z direction.

A cross-talk/leakage contribution that is 20 dB lower than a signal of interest results in a measurement uncertainty of about 1 dB.

Cable Flexing Ideally, the stressing of cables, connectors, and rotary joints should have no effect on a measurement. Practically, of course, there will always be some undesirable variation in amplitude and (especially) phase. The severity of the problem depends on the quality and condition of the components. If the errors are repeatable, one can use the reflectometer setup illustrated in Figure 19.7 to estimate the effect of cable flexing and to correct for it. In this procedure, the probe (or test antenna) is replaced with a reflectometer. The reflected signal is measured with respect to some reference point on the scan surface, where for convenience the amplitude and phase are set to 1.0 and 0°, respectively. The measured signal at other points on the surface will be given by $1 + 2\varepsilon$ for the amplitude and $2\delta\phi$ for the phase, where ε is the amplitude error and $\delta\phi$ is the phase error of the one-way path. An alternative method of measuring these errors is to use the three-cable method of Hess [46]. This method involves the use of three cables (with unknown properties) in pairs to determine the effect of cable flexing.

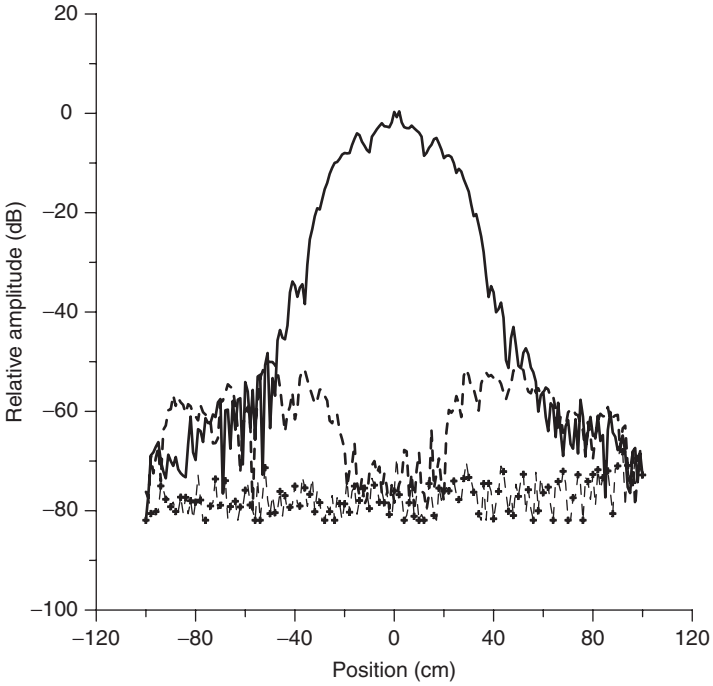

Figure 19.6 Sample leakage test results. The solid line represents the measured near field of the test antenna. The dashed line is a test result showing significant leakage problems. The $-+-+$ line is a test result showing more acceptable leakage levels.

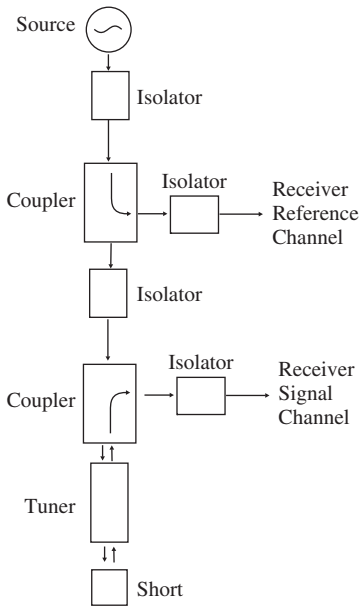

Figure 19.7 Reflectometer setup for estimating errors due to cable flexing.

Noise and Dynamic Range Parseval's theorem states that the root sum square (RSS) noise in the near field is equal to the RSS noise in the far field. The far-field peak is greater than the near-field peak by approximately the gain of the antenna. This implies that for a 30-dB gain antenna, if the noise level were at −40 dB relative to the near-field peak, we would expect it to be at about −70 dB relative to the far-field peak. A noise level that is 20 dB lower than a signal of interest results in a measurement uncertainty of about 1 dB.

Dynamic range is affected, not only by the noise level, but also by receiver saturation at high signal levels.

Nonlinearity Many receivers that have been manufactured, since about 1990, and used for antenna measurements are fairly linear in their optimal operating ranges. However, other receivers, especially those manufactured earlier, may exhibit significant nonlinearity. The effects of nonlinearity can be mitigated through comparison with a calibrated rotary vane or step attenuator. The system linearity can be evaluated by inserting a calibrated rotary vane attenuator. The setting of the attenuator is varied and the receiver output compared to the calibrated value of the attenuator. One obtains results similar to those in Table 19.2, where measurements are typically made relative to some reference point in the near field. (Table 19.2 is not intended to represent any particular receiving system.) In Table 19.2, column 2 represents the best value of the attenuation for the attenuator setting in column 1. Column 3 is the receiver reading for that attenuation. For example, for an attenuator setting of 30 dB, the calibrated attenuation is 30.02 dB and the receiver reading is −29.96 dB. That is, the receiver reading is 0.06 dB high since it should be −30.02 dB. This information can be used to generate a correction to the receiver output to obtain a calibrated value for each near-field data point.

Many modern devices, however, have better linearity than the rotary vane attenuator. In this case, it makes no sense to construct and use a table to correct the receiver output;

TABLE 19.2 Attenuator Calibration

Attenuator Setting (dB)	Calibrated Attenuator Value (dB)	Receiver Reading (dB)
0	0	0
2	2.00	− 2.00
4	4.00	− 4.00
6	6.01	− 6.01
8	8.01	− 8.01
10	10.01	−10.01
12	12.00	−12.00
14	14.00	−14.00
16	15.99	−15.99
18	17.99	−17.99
20	19.99	−19.99
25	24.98	−24.99
30	30.02	−29.96
35	35.02	−35.08
40	40.03	−40.12

however, this linearity test is still useful to detect abnormalities due to, for example, a faulty or improperly biased mixer.

Normalization There are several methods of determining the normalization ratios (b_0'/a_0 and b_0''/a_0). (1) Measure the insertion loss (a measurement of the power with the probe antenna and test antenna inserted in the circuit relative to the power with the generator and load connected directly together without the antennas) at a near-field reference point, as illustrated in Figure 19.8. The insertion loss measurement requires multiple connections and disconnections, so a connector of high quality is required. (2) In the gain substitution method, a known reference antenna is scanned to calibrate the measurement system. In this method we do not need to know the probe gain. (3) If the ohmic losses are negligible or can be calculated, then the gain can be determined from the directivity, Eq. (19.21). (4) The normalization can be accomplished using absolute power measurements.

To normalize the two polarization components relative to each other, it is necessary to refer them to a common signal. This can be done by measuring the signal at some near-field reference point of each component relative to the through connection (with the generator and load hooked directly together). Both the amplitude and phase must be determined in order to perform the probe correction accurately.

19.3.2 Planar Scanning Measurements

19.3.2.1 Overview of Planar Scanning In the planar scanning geometry, the test antenna is normally fixed and the probe antenna moves over the surface of a plane in front of the AUT. The probe and scanner act as an $x-y$ recorder. Because of truncation effects, the planar near-field scanning geometry is most useful for measuring moderately to highly directive antennas. For antennas with broad beams, the use of the planar near-field method is not advised since much of the energy will not be intercepted by a finite measurement

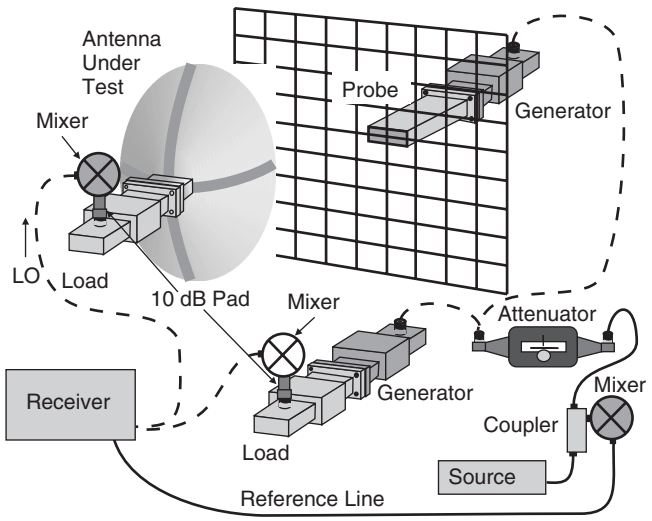

Figure 19.8 Illustration of the insertion loss measurement. The attenuator setting is usually higher for the generator-to-load connection to avoid nonlinearity effects and damage to the mixer.

region. Data are usually acquired "on the fly" in the scanning direction (e.g., the y direction). The probe is then stepped in the orthogonal direction (e.g., the x direction) and scanning reinitiated in the scanning direction.

19.3.2.2 Implementation

Alignment A properly aligned planar scanning measurement setup satisfies the following requirements. (1) The x and y axes are perpendicular. Furthermore, the plane over which the probe moves must be flat to within a small fraction of a wavelength (typically $0.01\lambda - 0.02\lambda$). (2) The probe z axis is perpendicular to the scan plane. The probe y axis must be parallel to the laboratory y axis. (3) The AUT coordinate system must be parallel to the laboratory coordinate system. (Translational displacement from the reference position produces only a phase factor in the far field, which is usually unimportant.)

The flatness required of the scan plane depends on the accuracy requirements and the nature of the error [47, Eqs. (53)–(61)]. For example, periodic position errors produce larger errors in the pattern, but these errors are concentrated in specific directions. The scan plane can be efficiently aligned or characterized by use of a laser tracker. Often, a mirror is positioned parallel to the scanner as a reference in the alignment of the probe and AUT.

The alignment of the probe may be accomplished by aligning a theodolite to the reference mirror mentioned above and using the autocollimation feature of the theodolite. Mirrors used for alignment should be of high quality with good optical surfaces and parallel front and back surfaces.

The AUT is generally aligned relative to an aligned probe.

Sampling Criteria Sampling considerations require that two data points be acquired for the shortest period in the measured data. Provided the measurements are acquired in a region where the evanescent (nonpropagating modes) are unimportant, increments of less than $\lambda/2$ in both x and y will generally satisfy the sampling criteria. However, there are error mechanisms that have periods that are less than a wavelength. In these cases, a sample spacing of less than $\lambda/2$ is necessary to prevent such errors from being aliased into the pattern.

Failure to satisfy the sampling criteria will lead to aliasing. One way to test for aliasing is to acquire data at intervals of much less than $\lambda/2$ (e.g., 0.1λ) and to check whether the pattern changes when fewer points (e.g., every other point) are used. Figure 19.9 shows how the root mean square error changes with spacing interval for a sample slotted waveguide array. Since this array had low sidelobes and measurements were required down to -60 dB, it was necessary to use spacing intervals of 0.4λ or less. The smaller spacing size is required because of the high frequency errors (see Figure 19.10) that occur due to probe–AUT multiple reflections. These errors are associated with the regular spacing between the slotted elements.

Scan Area Truncation The theory assumes an infinite scan plane and this is obviously not practical. Acquiring data over a finite area has two effects. First, the pattern beyond $\pm\theta_v$ is invalid [47], where

$$\theta_v = \arctan\left(\frac{L-a}{2d}\right) \tag{19.98}$$

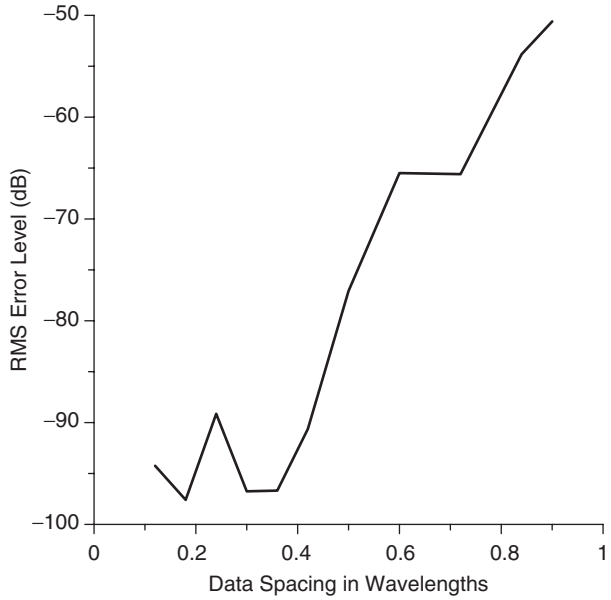

Figure 19.9 Example of the RMS error as a function of spacing size. Larger spacings lead to higher errors due to aliasing effects.

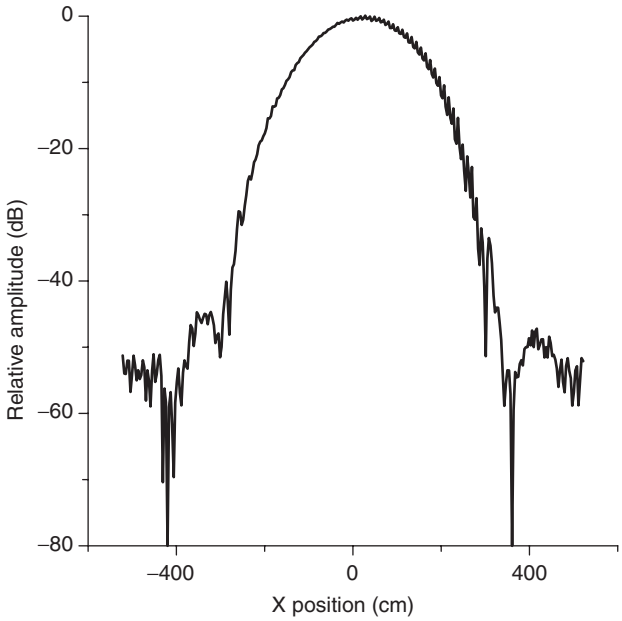

Figure 19.10 Near-field cut showing the ripple due to multiple reflections between the probe and the slots of the Ultralow Sidelobe Array (ULSA). The period of these ripples requires spacing sizes of less than about 0.38λ to avoid unacceptable aliasing errors.

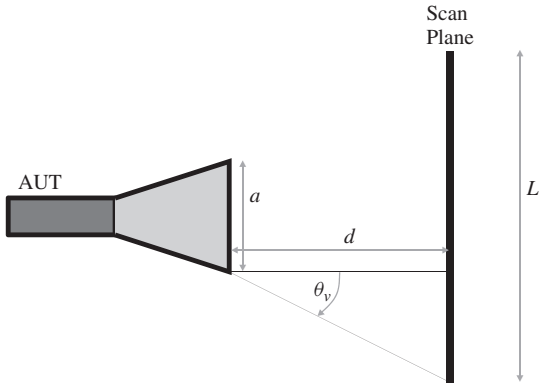

Figure 19.11 Illustration of the planar truncation geometry showing the angle of validity θ_v.

L is the scan length, a is the AUT diameter, and d is the separation distance between the AUT aperture and the scan plane (see Figure 19.11). Second, there are errors in the valid region due to ringing caused by the discontinuity at the edge of the scan plane. Yaghjian [48, p. 29] showed that this truncation error can be estimated from a knowledge of the measured data on the perimeter of the scan area. To determine whether the scan area is large enough, we set the data in the outer perimeter of the scan area to zero and observe how much the computed far field changes. As a rule of thumb, the scan area should be large enough so that measurements, at the edges, are at least 30 dB below (and preferably 40 dB or more below) the near-field peak.

Positioning Tolerances and Position Correction The fast Fourier transform, which provides an efficient near-field-to-far-field transform for the planar geometry, requires measurement points to be located on the plane $z = d$ in a regular grid, equispaced in x and equispaced in y. Errors can occur in the z coordinate (perpendicular to the scan plane) due to imperfections in the scanner (see Figure 19.12). Errors can occur in the step coordinate due to inertia in the scanner and errors in the y rails, which limit the step resolution (see Figure 19.13). Lastly, errors can occur in the scan coordinate due to errors in the x rails, the position encoders, the trigger timing accuracy, and the time to acquire a measurement. Newell [47, Eqs. (53)–(61)] and Yaghjian [48, Eq. (61)] may be consulted to estimate the errors in the far-field pattern due to position errors. Alternatively, one can use a laser tracker to determine the actual positions where the data are acquired and use a position-correction method such as that developed by Wittmann et al. [49] to perform an efficient near-field-to-far-field transform.

In addition, other sampling grids have been proposed [50–53]. The method of Wittmann et al. [49] can be used to process data acquired on a "nonstandard" grid.

Choosing a Separation Distance Several factors must be taken into account when choosing a probe–test antenna separation distance. First, we must ensure that evanescent (nonpropagating) modes do not contribute significantly to the measured near-field data (since it is extremely difficult to determine the response of the probe to these modes). A minimum separation of 3λ is often sufficient. The second consideration is that, as the separation distance increases, the valid region of the pattern decreases for a given scan area (see Eq. (19.98)). Thus we must choose a separation distance that allows adequate

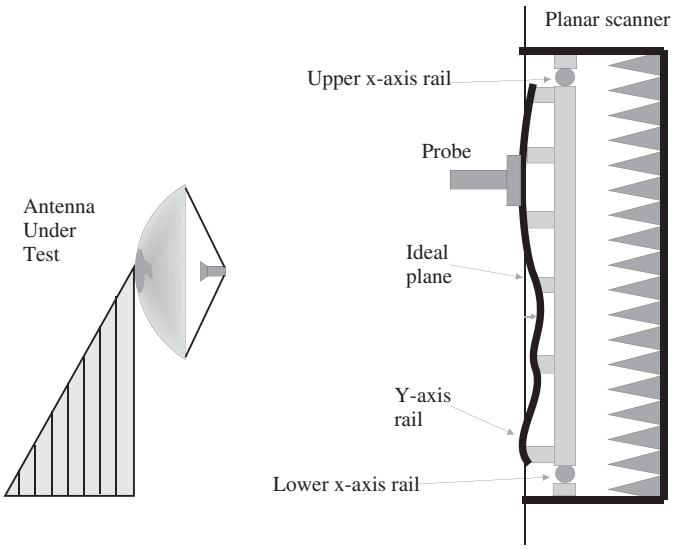

Figure 19.12 Illustration of z position error.

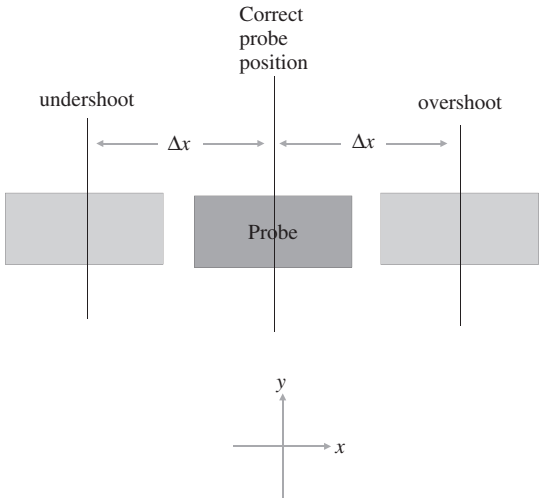

Figure 19.13 Illustration of the step position error. For the NIST planar scanner the step axis corresponds to the horizontal (x) axis.

pattern coverage. The final consideration is that of probe–AUT multiple reflections. When the signal travels from the transmitting antenna to the receiving antenna, not all the signal is received. Some of this signal is scattered from the receiving antenna back to the transmitting antenna and re-reflected to the receiving antenna. These reflections are not accounted for in the practical implementation of the theory. Multiple reflection errors generally increase with decreasing separation distance. It is preferable to choose a separation distance where the amplitude of the variation is smaller and where the gradient

is small. The multiple reflection effect can be estimated by taking measurements on two planes separated by $\lambda/4$, calculating the far field for each measurement, and computing the difference, direction by direction.

In choosing a separation distance, the need of smaller separation distances to increase pattern coverage (and improve signal to noise due to limited power) must be counterbalanced with the need to increase separation distance to decrease the effects of multiple reflections and evanescent modes.

Choosing a Probe As shown in Section 19.2.3.3, probe correction for planar near-field measurements is performed direction by direction after the transformation to the far field. One consequence is that if the probe has a null in its pattern, the uncertainty in the probe correction for that direction will be large. In planar scanning the probe should have good sensitivity in any direction for which we need an accurate determination of the AUT pattern.

Experience shows that the closer the probe and test antenna are in gain, the worse the multiple reflections will be. Thus the gain of the probe should be considerably less than that of the test antenna. However, if the gain is too small, then the insertion loss will be large and cannot be measured accurately. These factors lead us to generally choose a probe that has a gain that is approximately 20–30 dB less than that of the test antenna.

Finally, the return loss of the probe should be at least 10 dB (preferably 20 dB or more) to reduce the impedance mismatch. Corrections can be made for the impedance mismatch, but larger mismatch corrections are usually accompanied by larger measurement uncertainties.

Probe Correction The theory of probe correction (Section 19.2.3.3) requires the complex far-field patterns of two probes. The amplitude and phase of the second probe pattern must be known relative to the first probe pattern. If the second probe is the first probe rotated by 90° (as might be the case if one uses a linearly polarized probe to measure first one polarization and then the other), then the second probe pattern is the first probe pattern rotated by 90°. (For circularly polarized probe, the orthogonal polarization cannot be obtained by rotating the probe.) If the probe is a single antenna with more than one port (for different polarizations), then we must know the relative phase and amplitude between the ports. The amplitude difference can be calculated from the difference in gain between the ports. The phase difference must be measured (in the far field) by switching between the ports [43].

19.3.3 Spherical Scanning Measurements

19.3.3.1 Overview of Spherical Scanning A basic spherical scanning geometry is shown in Figure 19.3. There are a number of practical implementations of spherical scanning. (See Figures 19.14 and 19.15 for examples.) In all of them, the probe *effectively moves over the surface of a sphere*. We focus on the implementation of Figure 19.14 in which the test antenna is mounted on a roll-over-azimuth positioner. In this case, in contrast to the planar scanning case, it is the probe, rather than the AUT, that is fixed. The test antenna rotates in the two angular coordinates (see Figure 19.14). The spin angle χ is controlled at the probe, which is located on the laboratory z axis.

For AUTs with broad beams, the spherical near-field method is preferred because radiation in all directions is intercepted by the probe. Either θ' or φ' can be used as

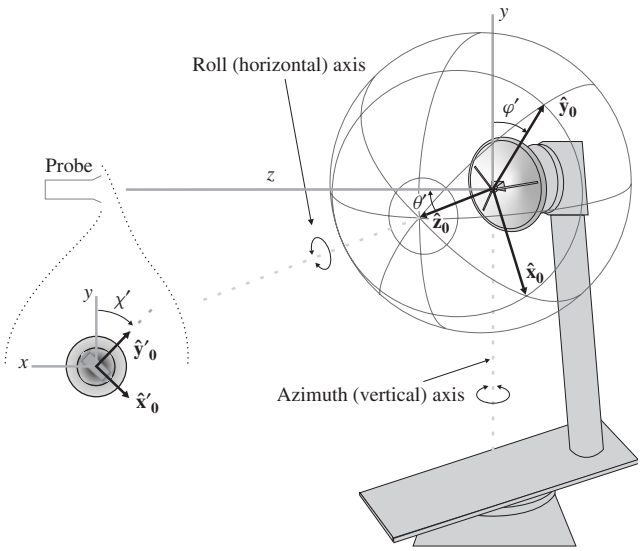

Figure 19.14 Spherical scanning with a roll-over-azimuth positioner. The inset shows the probe as viewed from the test antenna.

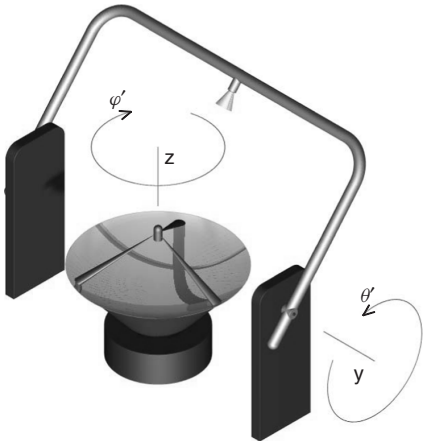

Figure 19.15 Spherical scanning with the probe on an arch and the test antenna on an azimuth rotator.

the scanning direction. The test antenna is then stepped in the orthogonal direction and scanning reinitiated in the scanning direction.

19.3.3.2 Implementation

Alignment A properly aligned roll-over-azimuth measurement setup satisfies the following requirements. (1) The azimuth (vertical) axis must be coincident with the laboratory y axis. The roll (horizontal) axis must be coincident with the laboratory z axis

when $\theta = 0$. (2) The AUT coordinate system must be coincident with the laboratory coordinate system when $\theta = 0$ and $\varphi = 0$. (3) The probe z axis must be coincident with the laboratory z axis. The probe y axis must be parallel to the laboratory y axis when $\chi = 0$.

Actual alignment procedures will vary from situation to situation. Because adjustments tend to be mutually dependent, it is necessary to iterate any procedure until further improvement is not practical. Perfect alignment is prevented, of course, by mechanical imperfections. For example, due to a lack of stiffness, it is generally not possible to maintain alignment of the z_a axis as a function of the roll angle φ. The alignment for spherical scanning is considerably more complex and time consuming than the alignment for planar or cylindrical scanning.

Sampling Criteria We must obtain enough data to determine the contributions of all relevant spherical modes. The magnitudes of the modal coefficients are observed to drop sharply for $n > N$, where $N \sim kr_0$ and r_0 is the radius of the minimum sphere. (The minimum sphere is the smallest sphere, centered on the origin of the laboratory coordinate system, that encloses the radiating parts of the AUT.) Sampling considerations then imply that

$$\Delta\theta, \Delta\varphi \leq \frac{2\pi}{2N+1} \tag{19.99}$$

To provide a margin of safety, N is often chosen so that $N = kr_0 + 10$. As in the planar case, undersampling leads to aliasing. A similar test can be performed for aliasing; that is, we obtain data with spacing about one-tenth that required by Eq. (19.99) and compare the results using all of the data with those obtained using every other point, then every third point, and so forth. In spherical scanning, oversampling can be used to reduce the effects of room reflections.

Scan Area Truncation In theory, data must be acquired over a complete sphere. Sometimes there are blockages (e.g., from mounting structures) so that obtaining data over a complete sphere becomes impossible. Acquiring data over a partial sphere has two effects. First, the pattern beyond $\pm\theta_v$ is invalid [26, p. 233], where

$$\theta_v = \theta_m - \arcsin\left(\frac{r_0}{d}\right) \tag{19.100}$$

where θ_m is the angle to which we obtain measured near-field data (see Figure 19.16), and d is the radius of the measurement sphere. Second, as in the planar case, there are errors in the valid region due to ringing. To determine whether the scan area is large enough, we set the data in the outer perimeter of the scan area to zero and observe how much the computed far field changes. As a rule of thumb, the scan area should be large enough so that measurements, at the edges, are at least 30 dB below (and preferably 40 dB or more below) the near-field peak. Some mitigation of truncation effects can be accomplished with a procedure such as that outlined in Wittmann et al. [54].

Positioning Tolerances and Position Correction The standard algorithm, which provides an efficient near-field-to-far-field transform for the spherical geometry, assumes that measurement points are located on the sphere $r = d$ in a regular grid, equispaced in θ and equispaced in φ. The position error must be small compared to the maximum

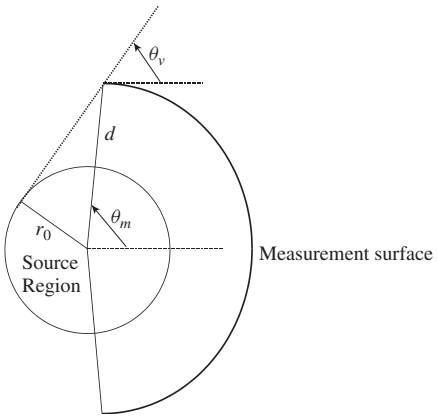

Figure 19.16 The spherical truncation geometry illustrating the angle of validity θ_v.

sample size allowed by Eq. (19.99). If one is able to determine the actual positions where the data are acquired, a position-correction method, such as that developed by Wittmann et al. [55], will provide an efficient near-field-to-far-field transform.

In addition, other sampling schemes have been proposed [56]. The method of Wittmann et al. [55] can be used to process data acquired on a "nonstandard" grid.

Choosing a Separation Distance In choosing the separation distance between the AUT and the probe (the measurement radius), we must consider the effects of probe–AUT multiple reflections and the effects of noise. An increased separation will reduce the effects of multiple reflections. However, increasing the separation tends to decrease the signal level so that the relative noise level is higher. Unlike the situation for planar scanning, an increase in the separation distance (measurement radius) decreases the effect of truncation for spherical scanning, Eq. (19.100). In spherical scanning, the separation between probe and AUT can never be less than the radius of the minimum sphere.

Choosing a Probe As shown in Section 19.2.4.3, the spherical transform relies on the probe having some special properties. The probe must have only spherical modes corresponding to $\mu = \pm 1$. That is, the probe response must have the form $A\cos(\chi + \chi_0)$, where χ is the rotation angle about the z axis of the probe. Also, the spherical transform theory assumes that the second probe (used for measuring the orthogonal polarization) is the same as the first probe but rotated 90°. Since a circularly polarized antenna rotated by 90° has the same polarization but a different tilt angle, this means we cannot use a circularly polarized probe in spherical scanning (but see the discussion after Eq. (19.75)).

As in the planar case, the gain of the probe should be considerably less than that of the test antenna. However, if the gain is too small, then the insertion loss will be large and cannot be measured accurately. These factors lead us to generally choose a probe that has a gain that is approximately 20–30 dB less than the test antenna.

Finally, the return loss of the probe should be at least 10 dB (preferably 20 dB or more) to reduce the impedance mismatch. Corrections can be made for the impedance mismatch, but larger mismatch corrections are usually accompanied by larger measurement uncertainties.

Probe Correction The theory of probe correction (Section 19.2.4.3) requires the complex far-field pattern of a single probe that is essentially linearly polarized. This probe is used in two χ orientations.

19.3.4 Cylindrical Scanning Measurements

19.3.4.1 Overview of Cylindrical Scanning

In common implementations of cylindrical scanning, both the probe and the AUT move. The AUT rotates in the angular coordinate Φ, while the probe is usually translated in the y (vertical) direction. The net result is equivalent to a probe moving over the surface of a cylinder about the test antenna (see Figure 19.4). The cylindrical scanning method is particularly useful for fan-beam antennas, which have a broad beam in one plane but a narrow beam in the orthogonal plane. For antennas with broad beams in both planes, the use of the spherical near-field method is preferred because radiation in all directions will be intercepted by the probe. Either Φ or y can be used as the scanning direction; that is, either the AUT is stepped in Φ and the probe scanned in y, or the probe is stepped in y and the AUT scanned in Φ.

19.3.4.2 Implementation

Alignment Cylindrical scanning is typically accomplished by use of an azimuth rotator for the Φ rotation and a vertical transport to move the probe in the laboratory y direction. The rotator is aligned so that its axis is coincident with the laboratory y axis. The probe is aligned so that $\hat{\mathbf{y}}_0' = \hat{\mathbf{y}}$ and $\hat{\mathbf{z}}_0' = -\hat{\mathbf{z}}$ at $\Phi = 0$ (see Figure 19.4).

Sampling Criteria For the angular coordinate the sampling requirement for cylindrical scanning is similar to that for the spherical scanning case (see Eq. (19.99)). For the translational coordinate the sampling requirement is similar to that for the planar scanning case (see Section 19.3.2.2). That is,

$$\begin{aligned} \Delta\Phi &\le \frac{2\pi}{2N+1} \\ \Delta y &\le \frac{\lambda}{2} \end{aligned} \tag{19.101}$$

where $N \sim k\rho_0$ and ρ_0 is the radius of the minimum cylinder. (The minimum cylinder is the smallest cylinder, centered on the y axis, that encloses the radiating parts of the AUT.)

Scan Area Truncation The theory requires data over an infinite cylinder. Acquiring data over a finite cylinder has two effects. First, the pattern beyond the cutoff angle is invalid. For the angular coordinate, the azimuthal angle of validity A_v is similar to the spherical case (Figure 19.16) and is given by

$$A_v = \Phi_m - \arcsin\left(\frac{\rho_0}{d}\right) \tag{19.102}$$

where Φ_m is the truncation angle for the near-field scan and d is the radius of the measurement cylinder. The elevation angle of validity E_v is similar to the planar angle of validity (Figure 19.11) and is given by

$$E_v = \arctan\left(\frac{L_y - a_y}{2d}\right) \tag{19.103}$$

where L_y is the scan length in the y direction, and a_y is the antenna extent in the y direction. Second, as in the planar case, there are errors in the valid region due to ringing. To determine whether the scan area is large enough, we set the data in the outer perimeter of the scan area to zero and observe how much the computed far field changes. As a rule of thumb, the scan area should be large enough so that measurements, at the edges, are at least 30 dB below (and preferably 40 dB or more below) the near-field peak.

Positioning Tolerances and Position Correction The standard algorithm, which provides an efficient near-field-to-far-field transform for the cylindrical geometry, requires measurement points to be located on the cylinder $\rho = d$ in a regular grid, equispaced in y and equispaced in Φ. The position error must be small compared to the maximum sample spacing allowed by Eq. (19.101). A probe-position correction algorithm for cylindrical scanning, such as those developed for spherical and planar scanning, has not been implemented to date, although such a scheme is certainly possible.

In addition, other sampling grids have been proposed [57].

Choosing a Separation Distance In choosing the separation distance between the test antenna and the probe (the measurement radius), we must consider the effects of probe–AUT multiple reflections, truncation, and noise. An increased separation will reduce the effects of multiple reflections. However, increasing the separation distance decreases the signal level, so that the relative noise level is higher. Increasing the separation distance has mixed results on the truncation in cylindrical scanning. It decreases the effects of truncation for the Φ direction (increases the angle of validity) but increases the truncation effect in the y direction (reduces the angle of validity). For cylindrical scanning, the separation between the probe and AUT cannot be less than the radius of the minimum cylinder.

Choosing a Probe As in the planar case, the gain of the probe should be considerably less than that of the test antenna. However, if the gain is too small, then the insertion loss will be large and cannot be measured accurately. These factors lead us to generally choose a probe that has a gain that is approximately 20–30 dB less than the test antenna.

The return loss of the probe should be at least 10 dB (preferably 20 dB or more) to reduce the impedance mismatch. Corrections can be made for the impedance mismatch, but larger mismatch corrections are usually accompanied by larger measurement uncertainties.

Probe Correction The theory of probe correction (Section 19.2.5.3) requires the complex far-field patterns of two probes. The amplitude and phase of the second probe pattern must be known relative to the first probe pattern. If the second probe is the first probe rotated by 90° (as might be the case if one uses a linearly polarized probe to measure first one polarization and then the other), then the second probe pattern is the first probe pattern rotated by 90°. (For a circularly polarized probe, the orthogonal polarization cannot be obtained by rotating the probe.) If the probe is a single antenna with more than one port (for different polarizations), then we must determine the relative phase and amplitude between the ports. The amplitude difference can be calculated from the difference in gain between the ports. The phase difference must be measured (in the far field) by switching between the ports [43].

19.3.5 Sources of Measurement Uncertainty

No measurement is truly complete without an uncertainty analysis that provides an estimate of how large the measurement error might be. A detailed analysis for estimating the errors in planar scanning has been presented by Newell [47]. For spherical scanning, an analysis of error sources has been done by Hansen [26, Chap. 6]. The sources of uncertainty are similar in all three scanning geometries. Tables 19.3 and 19.4 show the sources of uncertainty for test antenna gain and pattern, respectively. These tables are similar to the 18-term uncertainty table found in Newell [47].

Measurements of the AUT gain and the relative pattern share many sources of uncertainty. There are exceptions, however. The "probe relative pattern" uncertainty does not affect the resulting gain uncertainty of the AUT unless the AUT's main beam is steered off axis. Also, when the second probe is the same as the first probe but rotated 90°, the AUT relative pattern uncertainty is not affected by uncertainty in the "probe gain" or in the "impedance mismatch."

Near-field scanning has been used successfully to measure low sidelobe arrays [58, 59]. One example, the pattern of the ULSA for 3.0 GHz, is shown in Figure 19.17. The uncertainties for the measurement for this antenna are discussed in detail in Francis et al. [58]. The uncertainties relative to peak for directions other than the main beam and the grating lobe (at about 46°) are shown in Table 19.5. These values correspond to a coverage factor of 2. (Were we to assume a normal distribution, a coverage factor of 2 would correspond to a 95% (2σ) confidence level.) If an uncertainty source in Table 19.4 is not listed in Table 19.5 that is because its contribution is −100 dB or less. Table 19.6 shows the corresponding uncertainties versus sidelobe level.

TABLE 19.3 Sources of Uncertainty for Gain Measurement

Probe gain	Probe–AUT multiple reflections
Probe alignment	System nonlinearity
Probe relative pattern	System dynamic range
AUT alignment	Flexing cables
Normalization constant	Temperature (drift) effects
Impedance mismatch	Room scattering
Aliasing	Leakage and cross-talk
Measurement area truncation	Random errors
Probe position errors	

TABLE 19.4 Sources of Uncertainty for Relative Pattern Measurement

Probe polarization ratio	Probe position errors
Probe gain	Probe–AUT multiple reflections
Probe alignment	System nonlinearity
Probe relative pattern	System dynamic range
AUT alignment	Flexing cables
Normalization constant	Temperature (drift) effects
Impedance mismatch	Room scattering
Aliasing	Leakage and cross-talk
Measurement area truncation	Random errors

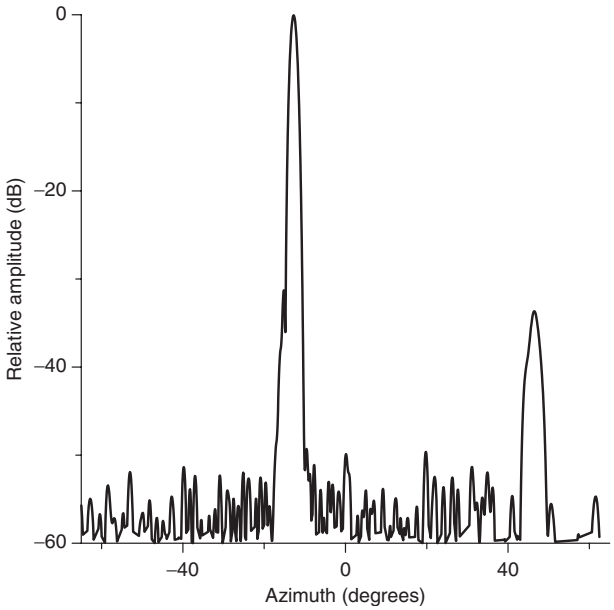

Figure 19.17 Azimuth cut of the far-field pattern of the ULSA as determined on the NIST planar near-field range. This pattern generally agrees with the ULSA pattern measured on a far-field range to within the uncertainties of measuremment. Note the grating lobe at 46°.

TABLE 19.5 Relative Pattern Uncertainties for the ULSA

Uncertainty Source	Uncertainty Level (dB relative to peak)
Probe–AUT multiple reflections	−65
Room scattering	−70
Cable flexing	−70
Position errors	−75
Random errors	−75
Leakage and cros-stalk	−75
Truncation	−90
Aliasing	−90
Root sum square	*−62*

TABLE 19.6 Relative Pattern Uncertainties Versus Sidelobe Level

Sidelobe Level (dB relative to peak)	Uncertainty (dB)	
−30	±0.25	
−45	+1.2,	−1.3
−55	+3.2,	−5.0
−60	+5.0,	−13.3

In the main beam region and the direction of the grating lobe, the probe–AUT multiple reflections are greater, and separate uncertainty tables are required for these directions.

19.4 SUMMARY

There are three geometries in which near-field scanning can be performed efficiently: planar, spherical, and cylindrical. As compared to far-field measurements, near-field scanning measurements use less real estate and provide a more controlled environment.

ACKNOWLEDGMENTS

The authors thank Jeff Guerrieri and Katie MacReynolds of the National Institute of Standards and Technology for their assistance in creating the figures and in acquiring near-field data. We also thank numerous reviewers for critical comments. In particular, we acknowledge detailed and lengthy discussions with Dr. Doren Hess of MI Technologies.

APPENDIX A: TRANSMITTING PROBE, RECEIVING TEST ANTENNA

Transmission formulas for cases when the probe transmits and the test antenna receives can be developed via slight generalization of the foregoing arguments. We list some key formulas.

Planar scanning: Corresponding to Eq. (19.42),

$$\frac{w(\mathbf{r})}{a_0'} = \int_{-\infty}^{\infty}\int_{-\infty}^{\infty} \mathbf{t}_\pi'(-\hat{\mathbf{k}}) \cdot \mathbf{s}_0(-\hat{\mathbf{k}}) \exp(i\mathbf{k}\cdot\mathbf{r}) \frac{d\alpha\, d\beta}{\gamma k} \tag{19.104}$$

Spherical scanning: Corresponding to Eqs. (19.67), (19.60), and (19.104),

$$\frac{w(r,\varphi,\theta,\chi)}{a_0'} = \sum_{n=1}^{\infty}\sum_{m=-n}^{n}\sum_{\mu=-n}^{n} \left[\tau_{n\mu}^{1\prime}(r) s_{nm}^1 + \tau_{n\mu}^{2\prime}(r) s_{nm}^2\right] D_{\mu m}^n(-\chi, -\theta, -\varphi) \tag{19.105}$$

$$\mathbf{s}_0(\hat{\mathbf{r}}) = \sum_{n=1}^{\infty}\sum_{m=-n}^{n} \left[s_{nm}^1 \mathbf{X}_{nm}^1(\hat{\mathbf{r}}) + s_{nm}^2 \mathbf{X}_{nm}^2(\hat{\mathbf{r}})\right] \tag{19.106}$$

$$\begin{aligned} \tau_{nm}^{1\prime}(r) &= \int_{-\infty}^{\infty}\int_{-\infty}^{\infty} \mathbf{t}_\pi'\left(-\hat{\mathbf{k}}\right) \cdot \mathbf{X}_{nm}^1(-\hat{\mathbf{k}}) \exp(i\gamma r) \frac{d\alpha\, d\beta}{\gamma k} \\ \tau_{nm}^{2\prime}(r) &= \int_{-\infty}^{\infty}\int_{-\infty}^{\infty} \mathbf{t}_\pi'(-\hat{\mathbf{k}}) \cdot \mathbf{X}_{nm}^2(-\hat{\mathbf{k}}) \exp(i\gamma r) \frac{d\alpha\, d\beta}{\gamma k} \end{aligned} \tag{19.107}$$

Cylindrical scanning: Corresponding to Eqs. (19.94), (19.87), and (19.132),

$$\frac{w(\mathbf{r})}{a_0'} = \sum_{n=-\infty}^{\infty} \int_{-\infty}^{\infty} \left[\tau_{n,-\beta}^{1\prime}(\rho)\, s_{n,-\beta}^1 + \tau_{n,-\beta}^{2\prime}(\rho)\, s_{n,-\beta}^2\right] \exp(in\Phi + i\beta y) \frac{d\beta}{k} \tag{19.108}$$

$$\mathbf{s}_0(\hat{\mathbf{r}}) = \sum_{n=-\infty}^{\infty} \left[s_{n,ky/r}^1 \boldsymbol{\Psi}_n^1(\hat{\mathbf{r}}) + s_{n,ky/r}^2 \boldsymbol{\Psi}_n^2(\hat{\mathbf{r}})\right] \tag{19.109}$$

$$\tau^{1'}_{n,-\beta}(\rho) = \int_{-\infty}^{\infty} \mathbf{t}'_{\pi}(-\hat{\mathbf{k}}) \cdot \boldsymbol{\Psi}^{1}_{n}(-\hat{\mathbf{k}}) \exp(i\gamma\rho) \frac{d\alpha}{\gamma}$$
$$\tau^{2'}_{n,-\beta}(\rho) = \int_{-\infty}^{\infty} \mathbf{t}'_{\pi}(-\hat{\mathbf{k}}) \cdot \boldsymbol{\Psi}^{2}_{n}(-\hat{\mathbf{k}}) \exp(i\gamma\rho) \frac{d\alpha}{\gamma} \tag{19.110}$$

In all geometries

$$\frac{w}{a'_0} = \frac{w'}{a_0} \tag{19.111}$$

when both the probe and test antenna are reciprocal.

APPENDIX B: SPECIAL PROBES

The use of $\mu = \pm 1$ probes leads to significant simplifications in the practical implementation of spherical near-field scanning techniques. These probes are often constructed by attaching a section of circular waveguide to a rectangular waveguide feed via a "smooth" transition. The guides are joined so they have a common axis and the transition region is designed so that the probe has reflection symmetry through two perpendicular planes. Figure 19.18 shows a $\mu = \pm 1$ probe intended for applications near 16 GHz.

The first few circular waveguide modes and their cutoff frequencies f_c are given in Table 19.7 [60, Sec. 2.3], where c is the speed of light and d is the inside diameter of the guide. Because of symmetry, the rectangular guide will not respond to $\mathrm{TE}_{\mu\nu}$ or

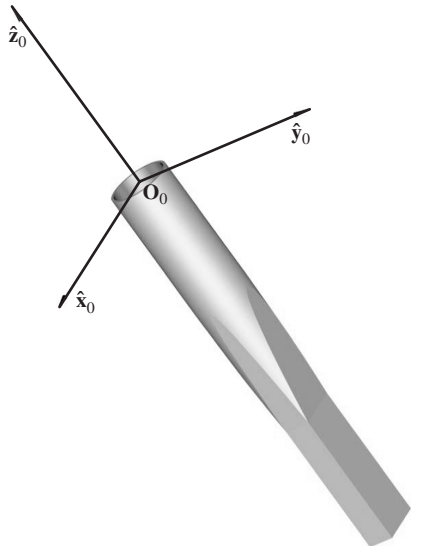

Figure 19.18 A Ku-band probe for spherical scanning measurements constructed from a section of WR-62 waveguide, followed by a symmetric transition to circular guide, followed by a section of circular waveguide. The length of each section is 5 cm. The inside diameter of the circular guide is 2 cm. The waveguide flange is not shown. The fiducial coordinate system has been chosen so that the origin is at the center of the circular aperture, the z axis is parallel to the probe axis, and the y axis is perpendicular to the broad side of the rectangular guide.

TABLE 19.7 Circular Waveguide Modes

Mode	f_c
TE_{11}	$1.841\dfrac{c}{\pi d}$
TM_{01}	$2.405\dfrac{c}{\pi d}$
TE_{21}	$3.054\dfrac{c}{\pi d}$
TE_{01}, TM_{11}	$3.832\dfrac{c}{\pi d}$
TE_{31}	$4.201\dfrac{c}{\pi d}$

$TM_{\mu v}$ modes when μ is even. To obtain the required $\mu = \pm 1$ dependence, the circular waveguide must filter out only the TE_{31} (and higher order) modes. When $d = 2.2$ cm, the TE_{31} mode is exponentially attenuated below 18.2 GHz and the probe will be useful over the full Ku band (12.4–18 GHz).

APPENDIX C: TRANSLATED PROBE COEFFICIENTS

C.1 Planar Geometry

The Kerns transmission formula (Eq. (19.42)) can be written

$$\frac{w'(\mathbf{r})}{a_0} = \int_{-\infty}^{\infty}\int_{-\infty}^{\infty} \left[\sigma_{\alpha\beta}^{1\prime}(z)t_{\alpha\beta}^{1} + \sigma_{\alpha\beta}^{2\prime}(z)t_{\alpha\beta}^{2}\right] \exp(i\alpha x + i\beta y)\frac{d\alpha\, d\beta}{\gamma k} \tag{19.112}$$

where the translated probe coefficients are

$$\begin{aligned} \sigma_{\alpha\beta}^{1\prime}(z) &= \left[\boldsymbol{\mathcal{P}} \cdot \mathbf{m}_{\alpha\beta}\right](0,0,z) = s_{\alpha\beta}^{1\prime}\exp(i\gamma z) \\ \sigma_{\alpha\beta}^{2\prime}(z) &= \left[\boldsymbol{\mathcal{P}} \cdot \mathbf{n}_{\alpha\beta}\right](0,0,z) = -s_{\alpha\beta}^{2\prime}\exp(i\gamma z) \end{aligned} \tag{19.113}$$

This form is directly comparable to Eqs. (19.67) and (19.94). Evaluation of the translated probe coefficients is considerably more complicated in the spherical and cylindrical geometries.

C.2 Spherical Geometry

The translated probe coefficients are defined in Eq. (19.66). Using the Kerns transmission formula (19.42) and plane wave representations for the spherical waves (19.58),

$$\begin{aligned} \sigma_{nm}^{1\prime}(r) &= \left[\boldsymbol{\mathcal{P}} \cdot \mathbf{m}_{n\mu}\right](r,0,0,0) = \int_{-\infty}^{\infty}\int_{-\infty}^{\infty} \mathbf{s}_{\pi}'(\hat{\mathbf{k}}) \cdot \mathbf{X}_{nm}^{1}(\hat{\mathbf{k}})\exp(i\gamma r)\frac{d\alpha\, d\beta}{\gamma k} \\ \sigma_{nm}^{2\prime}(r) &= \left[\boldsymbol{\mathcal{P}} \cdot \mathbf{n}_{n\mu}\right](r,0,0,0) = \int_{-\infty}^{\infty}\int_{-\infty}^{\infty} \mathbf{s}_{\pi}'(\hat{\mathbf{k}}) \cdot \mathbf{X}_{nm}^{2}(\hat{\mathbf{k}})\exp(i\gamma r)\frac{d\alpha\, d\beta}{\gamma k} \end{aligned} \tag{19.114}$$

Introducing the spherical-harmonic expansion

$$\mathbf{s}'_{\pi}(\hat{\mathbf{r}}) = \sum_{\nu=1}^{\infty} \sum_{\mu=-\nu}^{\nu} \left[s^{1'}_{\nu\mu} \mathbf{X}^1_{\nu\mu}(\hat{\mathbf{r}}) + s^{2'}_{\nu\mu} \mathbf{X}^2_{\nu\mu}(\hat{\mathbf{r}}) \right] \tag{19.115}$$

we have

$$\begin{aligned} \sigma^{1'}_{nm} &= \sum_{\nu=1}^{\infty} \left[B\,(\nu, -m|nm)\, s^{1'}_{\nu,-m} + C\,(\nu, -m|nm)\, s^{2'}_{\nu,-m} \right] \\ \sigma^{2'}_{nm} &= -\sum_{\nu=1}^{\infty} \left[C\,(\nu, -m|nm)\, s^{1'}_{\nu,-m} + B\,(\nu, -m|nm)\, s^{2'}_{\nu,-m} \right] \end{aligned} \tag{19.116}$$

with

$$\begin{aligned} B\,(\nu, -m|nm) &= \int_{-\infty}^{\infty} \int_{-\infty}^{\infty} \mathbf{X}^1_{\nu,-m}(\hat{\mathbf{k}}) \cdot \mathbf{X}^1_{nm}(\hat{\mathbf{k}}) \exp(i\gamma r) \frac{d\alpha\, d\beta}{\gamma k} \\ C\,(\nu, -m|nm) &= \int_{-\infty}^{\infty} \int_{-\infty}^{\infty} \mathbf{X}^2_{\nu,-m}(\hat{\mathbf{k}}) \cdot \mathbf{X}^1_{nm}(\hat{\mathbf{k}}) \exp(i\gamma r) \frac{d\alpha\, d\beta}{\gamma k} \end{aligned} \tag{19.117}$$

Products of vector spherical harmonics can be expanded in scalar spherical harmonics [24, Chap. 6]:

$$\begin{aligned} \mathbf{X}^1_{\nu,-m}(\hat{\mathbf{k}}) \cdot \mathbf{X}^1_{nm}(\hat{\mathbf{k}}) &= \sum_{\ell=|\nu-n|}^{\nu+n} b\,(\ell 0|\nu, -m, nm)\, Y_{\ell 0}\left(\hat{\mathbf{k}}\right) \\ \mathbf{X}^2_{\nu,-m}(\hat{\mathbf{k}}) \cdot \mathbf{X}^1_{nm}(\hat{\mathbf{k}}) &= \sum_{\ell=|\nu-n|}^{\nu+n} c\,(\ell 0|\nu, -m, nm)\, Y_{\ell 0}\left(\hat{\mathbf{k}}\right) \end{aligned} \tag{19.118}$$

so that

$$\begin{aligned} B\,(\nu, -m|nm) &= \sum_{\ell=|\nu-n|}^{\nu+n} \sqrt{\pi\,(2\ell+1)}\, f_{\ell}\,(kr)\, b\,(\ell 0|\nu, -m, nm) \\ C\,(\nu, -m|nm) &= \sum_{\ell=|\nu-n|}^{\nu+n} \sqrt{\pi\,(2\ell+1)}\, f_{\ell}\,(kr)\, c\,(\ell 0|\nu, -m, nm) \end{aligned} \tag{19.119}$$

where we have used Eqs. (19.48), and (19.50) and the fact that

$$Y_{nm}\,(\hat{\mathbf{z}}) = \sqrt{\frac{2n+1}{4\pi}} \delta_{m0} \tag{19.120}$$

The coefficients in Eq. (19.118) are [24, see Chap. 7]

$$b\left(\ell 0|\nu,-m,nm\right)=\sqrt{\frac{(2\ell+1)\,(2\nu+1)\,(2n+1)}{16\pi\,\nu\,(\nu+1)\,n\,(n+1)}}\left[\ell\,(\ell+1)-\nu\,(\nu+1)-n\,(n+1)\right]$$
$$\times\begin{pmatrix}\ell & \nu & n\\ 0 & 0 & 0\end{pmatrix}\begin{pmatrix}\ell & \nu & n\\ 0 & -m & m\end{pmatrix} \tag{19.121}$$

$$c\left(\ell 0|\nu,-m,nm\right)=-\sqrt{\frac{(2\ell+1)\,(2\nu+1)\,(2n+1)}{16\pi\,\nu\,(\nu+1)\,n\,(n+1)}}\sqrt{\left[\ell^2-(\nu-n)^2\right]\left[(\nu+n+1)^2-\ell^2\right]}$$
$$\times\begin{pmatrix}\ell-1 & \nu & n\\ 0 & 0 & 0\end{pmatrix}\begin{pmatrix}\ell & \nu & n\\ 0 & -m & m\end{pmatrix} \tag{19.122}$$

The 3-j symbols (which are scalars, not matrices) in these formulas may be computed recursively.

For a $\mu=\pm1$ probe, we require the special cases

$$b\left(\ell 0|\nu,\pm1,n,\mp1\right)=\sqrt{\frac{(2\ell+1)\,(2\nu+1)\,(2n+1)}{4\pi}}$$
$$\times\frac{\left[\ell\,(\ell+1)-\nu\,(\nu+1)-n\,(n+1)\right]^2}{4\nu\,(\nu+1)\,n\,(n+1)}\begin{pmatrix}\ell & \nu & n\\ 0 & 0 & 0\end{pmatrix}^2 \tag{19.123}$$

$$c\left(\ell 0|\nu,\pm1,n,\mp1\right)=\pm\sqrt{\frac{(2\ell+1)\,(2\nu+1)\,(2n+1)}{4\pi}}$$
$$\times\frac{\left[\ell^2-(\nu-n)^2\right]\left[(\nu+n+1)^2-\ell^2\right]}{4\nu\,(\nu+1)\,n\,(n+1)}\begin{pmatrix}\ell-1 & \nu & n\\ 0 & 0 & 0\end{pmatrix}^2 \tag{19.124}$$

The 3-j symbols in Eqs. (19.123) and (19.124) may be evaluated from the formulas

$$\begin{pmatrix}\ell & \nu & n\\ 0 & 0 & 0\end{pmatrix}=0 \tag{19.125}$$

when $\ell+\nu+n$ is odd, $\ell<|\nu-n|$, or $\ell>\nu+n$,

$$\sum_{\ell}(2\ell+1)\begin{pmatrix}\ell & \nu & n\\ 0 & 0 & 0\end{pmatrix}^2=1 \tag{19.126}$$

$$\xi_\ell\begin{pmatrix}\ell-1 & \nu & n\\ 0 & 0 & 0\end{pmatrix}^2=\xi_{\ell+1}\begin{pmatrix}\ell+1 & \nu & n\\ 0 & 0 & 0\end{pmatrix}^2 \tag{19.127}$$

$$\xi_\ell=\left[\ell^2-(\nu-n)^2\right]\left[(\nu+n+1)^2-\ell^2\right] \tag{19.128}$$

Asymptotic formulas are available for $\sigma_{nm}^{1\prime}$ and $\sigma_{nm}^{2\prime}$. Beginning with Eq. (19.114), a stationary-phase evaluation yields

$$\sigma_{nm}^{1\prime}(r) \underset{r\to\infty}{\sim} \mathbf{s}_\pi'(\hat{\mathbf{z}}) \cdot \int_{-\infty}^{\infty}\int_{-\infty}^{\infty} \mathbf{X}_{nm}^1(\hat{\mathbf{k}}) \exp(i\gamma r) \frac{d\alpha\, d\beta}{\gamma k}$$

$$\underset{r\to\infty}{\sim} 2\pi f_n(kr) \mathbf{s}_\pi'(\hat{\mathbf{z}}) \cdot \mathbf{X}_{nm}^1(\hat{\mathbf{z}}) \tag{19.129}$$

$$\sigma_{nm}^{2\prime}(r) \underset{r\to\infty}{\sim} \mathbf{s}_\pi'(\hat{\mathbf{z}}) \cdot \int_{-\infty}^{\infty}\int_{-\infty}^{\infty} \mathbf{X}_{nm}^2(\hat{\mathbf{k}}) \exp(i\gamma r) \frac{d\alpha\, d\beta}{\gamma k}$$

$$\underset{r\to\infty}{\sim} 2\pi g_n(kr)\, \mathbf{s}_\pi'(\hat{\mathbf{z}}) \cdot \mathbf{X}_{nm}^2(\hat{\mathbf{z}}) \tag{19.130}$$

where

$$\mathbf{X}_{nm}^1(\hat{\mathbf{z}}) = i\hat{\mathbf{z}} \times \mathbf{X}_{nm}^2(\hat{\mathbf{z}}) = \sqrt{\frac{2n+1}{16\pi}}\, (\hat{\mathbf{x}} \pm i\hat{\mathbf{y}})\, \delta_{m,\pm 1} \tag{19.131}$$

Formulas (19.129) and (19.130) provide a convenient numerical check in the evaluation of the translated probe coefficients. They also suggest, even for intermediate separations when the test antenna is in the "far field" of the probe, that practical probes are approximately $\mu = \pm 1$ and that on-axis properties of $\mathbf{s}_\pi'$ are most important.

C.3 Cylindrical Geometry

The translated probe coefficients are defined in Eq. (19.93). Using the Kerns transmission formula (19.42) and plane wave representations for the cylindrical waves (19.84),

$$\begin{aligned}
\sigma_{n\beta}^{1\prime}(\rho) &= \left[\mathcal{P} \cdot \mathbf{m}_{n\beta}\right](\rho, 0, 0) = \int_{-\infty}^{\infty} \mathbf{s}_\pi'(\hat{\mathbf{k}}) \cdot \boldsymbol{\Psi}_n^1(\hat{\mathbf{k}}) \exp(i\gamma\rho) \frac{d\alpha}{\gamma} \\
\sigma_{n\beta}^{2\prime}(\rho) &= \left[\mathcal{P} \cdot \mathbf{n}_{n\beta}\right](\rho, 0, 0) = \int_{-\infty}^{\infty} \mathbf{s}_\pi'(\hat{\mathbf{k}}) \cdot \boldsymbol{\Psi}_n^2(\hat{\mathbf{k}}) \exp(i\gamma\rho) \frac{d\alpha}{\gamma}
\end{aligned} \tag{19.132}$$

With the Fourier series representation

$$\mathbf{s}_\pi'(\hat{\mathbf{r}}) = \sum_{\nu=-\infty}^{\infty} \left[s_{\nu,ky/r}^{1\prime} \boldsymbol{\Psi}_\nu^1(\hat{\mathbf{r}}) + s_{\nu,ky/r}^{2\prime} \boldsymbol{\Psi}_\nu^2(\hat{\mathbf{r}})\right] \tag{19.133}$$

it follows that

$$\begin{aligned}
\sigma_{n\beta}^{1\prime}(\rho) &= \sum_{\nu=-\infty}^{\infty} \int_{-\infty}^{\infty} s_{\nu\beta}^{1\prime} \boldsymbol{\Psi}_\nu^1(\hat{\mathbf{k}}) \cdot \boldsymbol{\Psi}_n^1(\hat{\mathbf{k}}) \exp(i\gamma\rho) \frac{d\alpha}{\gamma} \\
&= \sqrt{2\pi} \sum_{\nu=-\infty}^{\infty} s_{\nu\beta}^{1\prime} \frac{1}{2\pi} \int_{-\infty}^{\infty} \Psi_{\nu+n}(\hat{\boldsymbol{\kappa}}) \exp(i\gamma\rho) \frac{d\alpha}{\gamma} \\
&= \sqrt{2\pi} \sum_{\nu=-\infty}^{\infty} s_{\nu\beta}^{1\prime} u_{\nu+n,\beta}(\rho\hat{\mathbf{z}})
\end{aligned}$$

$$= \frac{1}{\sqrt{2\pi}} \sum_{\nu=-\infty}^{\infty} s_{\nu\beta}^{1\prime} F_{\nu+n}(\kappa\rho) \tag{19.134}$$

where we have used Eqs. (19.76) and (19.79). Similarly,

$$\sigma_{n\beta}^{2\prime}(\rho) = -\frac{1}{\sqrt{2\pi}} \sum_{\nu=-\infty}^{\infty} s_{\nu\beta}^{2\prime} F_{\nu+n}(\kappa\rho) \tag{19.135}$$

Asymptotic formulas are available for $\sigma_{n\beta}^{1\prime}$ and $\sigma_{n\beta}^{2\prime}$ [12, 61]: Beginning with Eq. (19.134), a stationary-phase evaluation yields

$$\begin{aligned}
\sigma_{n\beta}^{1\prime}(\rho) &= \sum_{\nu=-\infty}^{\infty} \int_{-\infty}^{\infty} s_{\nu\beta}^{1\prime} \Psi_\nu(\hat{\boldsymbol{\kappa}}) \Psi_n(\hat{\boldsymbol{\kappa}}) \exp(i\gamma\rho) \frac{d\alpha}{\gamma} \\
&\underset{\rho\to\infty}{\sim} \sqrt{2\pi} \sum_{\nu=-\infty}^{\infty} s_{\nu\beta}^{1\prime} \frac{1}{2\pi} \int_{-\infty}^{\infty} \Psi_n(\hat{\boldsymbol{\kappa}}) \exp(i\gamma\rho) \frac{d\alpha}{\gamma} \\
&\underset{\rho\to\infty}{\sim} \sqrt{2\pi} \sum_{\nu=-\infty}^{\infty} s_{\nu\beta}^{1\prime} u_{n\beta}(\rho\hat{\mathbf{z}}) \\
&\underset{\rho\to\infty}{\sim} \frac{1}{\sqrt{2\pi}} F_n(\kappa\rho) \sum_{\nu=-\infty}^{\infty} s_{\nu\beta}^{1\prime}
\end{aligned} \tag{19.136}$$

and similarly,

$$\sigma_{n\beta}^{2\prime}(\rho) \underset{\rho\to\infty}{\sim} -\frac{1}{\sqrt{2\pi}} F_n(\kappa\rho) \sum_{\nu=-\infty}^{\infty} s_{\nu\beta}^{2\prime} \tag{19.137}$$

But

$$\mathbf{s}_\pi'\left(\frac{\kappa}{k}\hat{\mathbf{z}} + \frac{\beta}{k}\hat{\mathbf{y}}\right) = \frac{1}{\sqrt{2\pi}} \sum_{\nu=-\infty}^{\infty} \left(s_{\nu\beta}^{1\prime}\hat{\boldsymbol{\Phi}} - i s_{\nu\beta}^{2\prime}\hat{\boldsymbol{\Theta}}\right) \tag{19.138}$$

so that

$$\begin{aligned}
\sigma_{n\beta}^{1\prime}(\rho) &\underset{\rho\to\infty}{\sim} F_n(\kappa\rho)\hat{\boldsymbol{\Phi}} \cdot \mathbf{s}_\pi'\left(\frac{\kappa}{k}\hat{\mathbf{z}} + \frac{\beta}{k}\hat{\mathbf{y}}\right) \\
\sigma_{n\beta}^{2\prime}(\rho) &\underset{\rho\to\infty}{\sim} -i F_n(\kappa\rho)\hat{\boldsymbol{\Theta}} \cdot \mathbf{s}_\pi'\left(\frac{\kappa}{k}\hat{\mathbf{z}} + \frac{\beta}{k}\hat{\mathbf{y}}\right)
\end{aligned} \tag{19.139}$$

Formulas (19.139) provide a convenient numerical check in the evaluation of the translated probe coefficients. They also suggest, even for intermediate separations when the test antenna is in the "far field" of the probe, that the $\Phi = 0$ cut of $\mathbf{s}_\pi'$ is most important.

REFERENCES

1. J. S. Hollis, T. J. Lyon, and L. Clayton, *Microwave Antenna Measurements*, 3rd ed., Scientific-Atlanta, Inc., 1985.

2. D. M. Kerns and E. S. Dayhoff, Theory of diffraction in microwave interferometry, *J. Res. Natl. Bur. Stand.*, Vol. 64B, pp. 1–13, January–March 1960.
3. D. M. Kerns, Analytical techniques for the correction of near-field antenna measurements made with an arbitrary but known antenna, presented at the URSI-IRE Meeting, Washington, DC, 29 April–2 May, 1963.
4. D. M. Kerns, Correction of near-field antenna measurements made with an arbitrary but known antenna, *Electron. Lett.*, Vol. 6, pp. 346–347, 28 May, 1970.
5. J. Brown and E. B. Jull, The prediction of aerial radiation patterns from near-field measurements, *Proc. Inst. Elec. Eng.*, pp. 635–644, November 1961.
6. F. Jensen, Electromagnetic near-field far-field correlations, Ph.D. dissertation, Technical University of Denmark, Lyngby, 1970.
7. F. Jensen, On the probe compensation for near-field measurements on a sphere, *Arch. Elek. Übertagung.*, Vol. 29, pp. 306–308, July/August 1975.
8. F. Holm Larsen, Probe correction of spherical near-field measurements, *Electron. Lett.*, Vol. 13, pp. 393–395, July 1977.
9. P. F. Wacker, Non-planar near-field measurements: spherical scanning, National Bureau of Standards (U.S.), NBSIR 75-809, June 1975.
10. W. M. Leach, Jr. Probe compensated near-field measurements on a cylinder, Ph.D. dissertation, Georgia Institute of Technology, Atlanta, GA, August 1972.
11. W. M. Leach, Jr. and D. T. Paris, Probe compensated near-field measurements on a cylinder, *IEEE Trans. Antennas Propag.*, Vol. 21, pp. 435–445, July 1973.
12. A. D. Yaghjian, Near-field antenna measurements on a cylindrical surface: A source scattering-matrix approach, National Bureau of Standards Tech. Note 696, September 1977.
13. E. S. Gillespie (Ed.), Special Issue on Near-Field Scanning Techniques, *IEEE Trans. Antennas Propag.*, Vol. 36, pp. 725–901, June 1988.
14. R. C. Baird, A. C. Newell, and C. F. Stubenrauch, A brief history of near-field measurements at the National Bureau of Standards, *IEEE Trans. Antennas Propag.*, Vol. 36, pp. 727–733, June 1988.
15. J. E. Hansen and F. Jensen, Spherical near-field scanning at the Technical University of Denmark, *IEEE Trans. Antennas Propag.*, Vol. 36, pp. 734–739, June 1988.
16. E. B. Joy, A brief history of the development of the near-field measurement technique at the Georgia Institute of Technology, *IEEE Trans. Antennas Propag.*, Vol. 36, pp. 740–745, June 1988.
17. A. D. Yaghjian, An overview of near-field antenna measurements, *IEEE Trans. Antennas Propag.*, Vol. 34, pp. 30–45, January 1986.
18. J. Appel-Hansen, E. S. Gillespie, T. G. Hickman, and J. D. Dyson, Antenna measurements, in *The Handbook of Antenna Design*, A. W. Rudge, K. Milne, A. D. Olver, and P. Knight (Eds.), Peter Peregrinus Ltd., London, 1982, Chap. 8.
19. D. M. Kerns, Scattering matrix description and nearfield measurements of electroacoustic transducers, *J. Acoust. Soc. Am.*, Vol. 57, pp. 497–507, February 1975.
20. A. D. Yaghjian, Simplified approach to probe-corrected spherical near-field scanning, *Electron. Lett.*, Vol. 20, pp. 195–196, 1 March 1984.
21. R. C. Wittmann, Probe-corrected spherical near-field scanning in acoustics, *IEEE Trans. Instrum. Meas.*, Vol. 41, pp. 17–21, February 1992.
22. T. B. Hansen, Probe-corrected near-field measurements on a truncated cylinder, *J. Acoust. Soc. Am.*, Vol. 119, pp. 792–807, February 2006.
23. A. D. Yaghjian and R. C. Wittmann, The receiving antenna as a linear differential operator: application to spherical near-field measurements, *IEEE Trans. Antenna Propag.*, Vol. 33, pp. 1175–1185, November 1985.

24. R. C. Wittmann and C. F. Stubenrauch, Spherical near-field scanning: Experimental and theoretical studies, National Institute of Standards and Technology, NISTIR 3955, July 1990.
25. D. M. Kerns, Plane-wave scattering matrix theory of antennas and antenna–antenna interactions, National Bureau of Standards (U.S.) Monograph 162, 1981.
26. J. E. Hansen (Ed.), *Spherical Near-Field Antenna Measurements*, Peter Peregrinus Ltd., London, 1988.
27. V. Rokhlin, and M. Tygert, Fast algorithms for spherical harmonic expansions, *SIAM J. Sci. Comp.*, Vol. 27, pp. 1903–1928, 2006.
28. T. B. Hansen and A. D. Yaghjian, *Plane-Wave Theory of Time Domain Fields*, IEEE Press, Piscataway, NJ, 1999.
29. A. Messiah, *Quantum Mechanics*, Vol. 2, North-Holland Publishing Company, Amsterdam, 1963.
30. D. M. Kerns and R. W. Beatty, *Basic Theory of Waveguide Junctions and Introductory Microwave Network Analysis*, Pergamon, Oxford, UK, 1967.
31. *IEEE Standard Definitions of Terms for Antennas*, IEEE Std 145- 1993.
32. A. C. Newell, R. D. Ward, and E. J. McFarlane, Gain and power parameter measurements using planar near-field techniques, *IEEE Trans. Antennas Propag.*, Vol. 36, pp. 792–803, June 1988.
33. A. D. Yaghjian, Efficient computation of antenna coupling and fields within the near-field region, *IEEE Trans. Antennas Propag.*, Vol. 30, pp. 113–128, January 1982.
34. C. Müller, *Foundations of the Mathematical Theory of Electromagnetic Waves*, Springer-Verlag, Berlin, 1969.
35. R. C. Wittmann, Spherical wave operators and the translation formulas, *IEEE Trans. Antennas Propag.*, Vol. 36, pp. 1078–1087, August 1988.
36. J. D. Jackson, *Classical Electrodynamics*, 3rd ed., John Wiley & Sons, Hoboken NJ, 1999.
37. M. E. Rose, *Elementary Theory of Angular Momentum*, John Wiley & Sons, Hoboken, NJ, 1957.
38. M. Tinkham, *Group Theory and Quantum Mechanics*, McGraw-Hill, New York, 1964.
39. A. R. Edmonds, *Angular Momentum in Quantum Mechanics*, 3rd ed., Princeton University Press, Princeton, NJ, 1974.
40. M. Abramowitz and I. E. Stegun (Eds.), *Handbook of Mathematical Functions*, National Bureau of Standards (U.S.) Applied Mathematics Series Vol. 55, 1972.
41. I.S. Gradshteyn, and I. M. Ryzhik. *Table of Integrals, Series, and Products*, Academic Press, San Diego, 1980.
42. A. G. Repjar, A. C. Newell, and M. H. Francis, Accurate determination of planar near-field correction parameters for linearly polarized probes, *IEEE Trans. Antennas Propag.*, Vol. 36, pp. 855–868, June 1988.
43. A. C. Newell, M. H. Francis, and D. P. Kremer, The determination of near-field correction parameters for circularly polarized probes, *Proc. Antenna Measurement Tech. Assoc.*, Vol. 6, pp. 3A3-2–3A3-29, 1984.
44. A. C. Newell, D. P. Kremer, and J. R. Guerrieri, Improvements in polarization measurements of circularly polarized antennas, *Proc. Antenna Measurement Tech. Assoc.*, Vol. 11, pp. 1-30–1-35, October 1989.
45. D. P. Kremer, W. J. Parker, A. C. Newell, and F. Mayo-Wells, Tests of the fire performance of microwave absorber, *Proc. Antenna Measurement Tech. Assoc.*, Vol. 12, pp. 3–19, 1990.
46. D. W. Hess, Principle of the three-cable method for compensation of cable variations, *Proc. Antenna Measurement Tech. Assoc.*, Vol. 14, pp. 10-26–10-32, 1992.
47. A. C. Newell, Error analysis techniques for planar near-field measurements, *IEEE Trans. Antennas Propag.*, Vol. 36, pp. 754–768, June 1988.

48. A. D. Yaghjian, Upper-bound errors in far-field antenna parameters determined from planar near-field measurements, National Bureau of Standards Tech. Note 667, October 1975.
49. R. C. Wittmann, B. K. Alpert, and M. H. Francis, Near-field antenna measurements using nonideal measurements locations, *IEEE Trans. Antennas Propag.*, Vol. 46, pp. 716–722, May 1998.
50. Y. Rahmat-Samii, V. Galindo-Israel, and R. Mittra, A plane-polar approach for far-field construction from near-field measurements, *IEEE Trans. Antennas Propag.*, Vol. 28, pp. 216–230, March 1980.
51. R. G. Yaccarino, Y. Rahmat-Samii, and L. I. Williams, The bi-polar planar near-field measurement technique—Part II: Near-field to far-field transformation and holographic imaging methods, *IEEE Trans. Antennas Propag.*, Vol. 42, pp. 196–204, February 1994.
52. L. I. Williams, Y. Rahmat-Samii, and R. G. Yaccarino, The bi-polar planar near-field measurement technique—Part I: Implementation and measurement comparisons, *IEEE Trans. Antennas Propag.*, Vol. 42, pp. 184–195, February 1994.
53. O. M. Bucci, F. D'Agostino, C. Gennarelli, G. Riccio, and C. Savarese, Probe compensated far-field reconstruction by near-field planar spiral scanning, *Proc. IEE Microwave Antennas Propag.*, Vol. 149, pp. 119–123, April 2002.
54. R. C. Wittmann, C. F. Stubenrauch, and M. H. Francis, Spherical scanning measurements using truncated data sets, *Proc. Antenna Measurement Techn. Assoc.*, Vol. 24, pp. 279–283, November 2002.
55. R. C. Wittmann, B. K. Alpert, and M. H. Francis, Near-field, spherical scanning antenna measurements with non-ideal probe locations, *IEEE Trans. Antennas Propag.*, Vol. 52, pp. 2184–2186, August 2004.
56. O. M. Bucci, F. D'Agostino, C. Gennarelli, G. Riccio, and C. Savarese, Field recovery over a sphere from a minimum number of data over a spiral, in *ANTEM 2000*, Winnipeg, Canada, July 2000, pp. 187–190.
57. O. M. Bucci, C. Gennarelli, G. Riccio, and C. Savarese, Probe compensated NF-FF transformation with helicoidal scanning, *J. Electromagn. Waves Appl.*, Vol. 14, pp. 531–549, 2000.
58. M. H. Francis, A. C. Newell, K. R. Grimm, J. Hoffman, and H. Schrank, Planar near-field measurement of low sidelobe antennas, *J. Res. Natl. Inst. Stand. Tech.*, Vol. 99, pp. 143–167, March–April 1994.
59. M. H. Francis, A. C. Newell, K. R. Grimm, J. Hoffman, and H. Schrank, Comparison of ultralow-sidelobe antenna far-field patterns using the planar-near-field method and the far-field method, *IEEE Antennas Propag. Mag.*, Vol. 37, pp. 7–15, December 1995.
60. N. Marcuvitz, *Waveguide Handbook*, McGraw-Hill, New York, 1951.
61. G. V. Borgiotti, Integral equation formulation for probe corrected far-field reconstruction from measurements on a cylinder, *IEEE Trans. Antennas Propag.*, Vol. 26, pp. 572–578, July 1978.